

CALIFORNIA STATE UNIVERSITY, NORTHRIDGE

Near Real-Time Monitoring of Global Evapotranspiration
and its Application to Water Resource Management

A thesis submitted in partial fulfillment of the requirements
For the degree of Master of Science in Geographic Information Science

By
Gregory H. Halverson

December 2018

The thesis of Gregory H. Halverson is approved:

Dr. Joshua Fisher

Date

Dr. Soheil Boroushaki

Date

Dr. Regan Maas, Chair

Date

California State University, Northridge

Acknowledgements

I would like to express my gratitude to my advisor and chair, Dr. Regan Maas, and graduate advisor and committee member, Dr. Soheil Boroushaki, of the California State University, Northridge, Department of Geography, for supervising the development and submission of this master's thesis. Dr. Maas taught me the science and art of investigating data through statistics and data science and introduced me to the R language. Dr. Boroushaki taught me the use of Leaflet and supervised the development and testing of the WebGIS system described in this master's thesis.

I would like to express my gratitude to my mentor and patron, Dr. Joshua Fisher of NASA Jet Propulsion Laboratory for keeping me as an intern at JPL and formulating, directing, and funding the development and testing of the system described in this master's thesis. Dr. Joshua Fisher is the Science Lead of the ECOSTRESS mission and creator of the PT-JPL model. Following his role as Science Advisor of my first NASA DEVELOP term, Dr. Fisher inspired and encouraged me to develop this project both as a comprehensive exercise in scientific computing and an introduction to the world of environmental science. Dr. Fisher advised my presentations of the research described in this thesis to the Carbon Club at Jet Propulsion Laboratory, the Annual Earth Science Applications Showcase at NASA Headquarters, and the American Geophysical Union Fall Meeting.

I would like to express my gratitude to my advisor and patron, Dr. Christine Lee of the Western Water Applications Office at NASA Jet Propulsion Laboratory for funding the development and deployment of the system described in this master's thesis. Dr. Christine Lee is the Applications Lead of the ECOSTRESS mission. Dr. Lee was the Science Advisor of my second NASA DEVELOP term and introduced me to the world of the ECOSTRESS mission and diurnal land-surface temperature. Dr. Lee encouraged and funded my presentation of ECOSTRESS at the Annual Earth Science Applications Showcase at NASA Headquarters. Dr. Lee encouraged me to continue development of this project and present it at the American Geophysical Union Fall Meeting.

I would like to express my gratitude to Molly Magnuson and John Longworth of the New Mexico Office of the State Engineer for agreeing to partner as early adopters of the system described in this master's thesis. John Longworth directed the formulation of the WebGIS system described in this document and its applications to resource management.

I would like to express my gratitude to my collaborator, Dr. Laura Jewell, of NASA Jet Propulsion Laboratory. Dr. Jewell is the Algorithm Development Lead of the ECOSTRESS L3/L4 products. Over the course of formulation, implementation, and testing of this project, we have exchanged a great deal of ideas, code, and results to implement a system suitable for both the ECOSTRESS and MODIS data products described in this master's thesis.

I would like to thank my predecessors, Dr. Greg Moore and Dr. Manish Verma, of NASA Jet Propulsion Laboratory, for adapting Dr. Youngryel Ryu's net radiation model and Dr. Joshua Fisher's evapotranspiration model to MODIS using data provided by the Lawrence

Berkeley National Laboratory. Their system in MATLAB was the reference for the system I developed in Python for this master's thesis. Dr. Moore and Dr. Verma introduced me to the world of surface energy balance calculation.

I would like to express my gratitude to my professor Dr. Steven Graves and Dr. Helen Cox of the California State University, Northridge, Department of Geography, for bringing me into the department and introducing me to the use of GIS software. Dr. Steven Graves introduced me to the department and advised in starting my master's term. Dr. Cox taught me the science and art of remote sensing the environment using satellite and aerial imagery and unmanned aerial vehicles. Following my remote sensing class, Dr. Cox encouraged me to continue studying the science and application of land-surface temperature and the surface energy balance.

I would like to express my gratitude to Trevor McDonnell, Sol Kim, and Augustin Muniz, of NASA DEVELOP for their work in the formulation and proof of concept of this project in the NASA DEVELOP project that preceded my first NASA DEVELOP term. Trevor McDonald developed a prototype of the WebGIS system described here through his work with me in NASA DEVELOP and taught me the use of GeoServer. Sol Kim demonstrated the conversion of MODIS swath data to MODIS land tiles using HEG through his work with NASA DEVELOP, from which I based the region matching and projection system used in this project using SciPy. Augustin Muniz demonstrated the automation of wget for acquisition of MODIS data from the LP-DAAC, from which I developed the data acquisition system used in this project.

I would like to express my gratitude to my team members from my second develop term, Savannah Cooley, Steven Pestana, and Mark Barker of NASA DEVELOP. I was the Team Lead for my second NASA DEVELOP term, with their support. They taught me how to lead a science team and provided support in my presentation of our project to the Annual Earth Science Applications Showcase at NASA headquarters. Savannah Cooley is advancing the science and applications of the ECOSTRESS mission and has served as an initial end user for the MODIS data product described in this master's thesis project. Savannah Cooley has since become affiliated with the Western Water Applications office and has made significant contributions toward the impact assessment of the New Mexico applications described here.

I would like to express my gratitude to my supervisors, Nick Rousseau and Brittany Zajic of NASA DEVELOP for placing me into and guiding me through my DEVELOP terms, which formed the basis for this master's thesis. Nick Rousseau was the Center Lead of the NASA DEVELOP JPL Node and advised extensively in my development of leadership abilities in my second DEVELOP term. Brittany Zajic was the Assistant Center Lead at the NASA DEVELOP JPL Node. She introduced me to the world of the Jet Propulsion Laboratory and advised on my presentation to the Annual Earth Science Applications Showcase at NASA Headquarters.

I would like to express my gratitude to my coworkers, Munish Sikka, Adam Purdy, and Dr. Eric Stofferahn, of NASA Jet Propulsion Laboratory for their continual advice and guidance. Munish Sikka has advised and collaborated extensively in the development and

testing of this system. Adam Purdy has advised extensively in the science of the PT-JPL model and its relationship to soil moisture and soil heat flux.

I would like to express my gratitude to my professor, Dr. Amalie Orme, of the California State University, Northridge, Department of Geography, for introducing me to the world of Geography and field studies. Dr. Orme supervised my study of geodesy, surveying, plant and soil measurement, and photogrammetry by means of unmanned aerial vehicles.

I would like to thank my professors, David Deis and Dr. James Craine, of the California State University, Northridge, Department of Geography, for teaching me the art of cartography and map making. Professor Deis encouraged me to present my studies of land-surface temperature at the California Geographical Society conference. Dr. Craine taught me the artistic representation of geographic information.

I would like to express my gratitude to my cohort, Justine Maybrun, of the California State University, Northridge, Department of Geography, for her extensive guidance and collaboration in the study of geospatial data science, environmental science, the art of cartography, and for introducing me to the world of field studies and lab science.

I would like to express my gratitude to my sister, Catherine Halverson, of Mt. Saint Mary's University, Los Angeles, for introducing me to the California State University, Northridge, Department of Geography. Catherine encouraged me to apply my computer science skills to the study of environment science and introduced me to the world of Geographic Information Science.

The research presented in this master's thesis derives partially from three NASA DEVELOP projects:

New Mexico Water Resources I, Summer 2015

New Mexico Water Resources II, Fall 2015

Costa Rica Agriculture I, Summer 2016

Any opinions, findings, and conclusions or recommendations expressed in this material are those of the author(s) and do not necessarily reflect the views of the National Aeronautics and Space Administration. This material is based upon work supported by NASA through contract NNL11AA00B and cooperative agreement NNX14AB60A.

Table of Contents

Signature Page	ii
Acknowledgements.....	iii
Table of Figures.....	ix
Table of Tables	x
Table of Equations	xi
Abstract	xiii
1 Introduction.....	1
1.1 Partnership with the New Mexico Office of the State Engineer.....	4
1.2 Collaboration with the ECOSTRESS Mission.....	5
2 Background.....	6
2.1 Evapotranspiration.....	6
2.2 Water Capacity of the Air.....	6
2.3 Cycles of the Land Surface.....	7
2.3.1 Surface Energy Budget	8
2.3.2 Water Cycle.....	9
2.3.3 Carbon Cycle.....	10
3 Literature Review.....	12
3.1 Examples of Operational Water Monitoring Systems.....	12
3.1.1 GLAM.....	12
3.1.2 GIDMaPS.....	14
3.2 Approaches to Remote Sensing of Evapotranspiration	14
3.2.1 SEBS.....	15
3.2.2 METRIC.....	16
3.2.3 ALEXI.....	16
3.2.4 BESS.....	17
3.2.5 PT-JPL	19
4 Processing Overview.....	22
5 Data Acquisition	23
5.1 Region Intersection.....	23
5.1.1 MODIS Land Tiles	23
5.1.2 MODIS Swaths.....	25

5.1.3	Polygon Intersection.....	28
5.2	Address Resolution	29
5.2.1	LP-DAAC	29
5.2.2	LAADS	30
5.2.3	NCEP	30
5.2.4	Amazon Web Services	30
5.3	Data Transfer	31
6	Processing	32
6.1	Data Ingest.....	32
6.1.1	Solar Zenith Angle	34
6.1.2	IGBP Land Cover Classification.....	35
6.1.3	Köppen-Geiger Climate Classification	35
6.1.4	Aerosol Optical Thickness.....	36
6.1.5	Cloud Optical Thickness	36
6.1.6	Cloud Top Height.....	37
6.1.7	Cloud Fraction	37
6.1.8	Albedo	37
6.1.9	Surface Pressure.....	40
6.1.10	Air Temperature.....	40
6.1.11	Dew-Point Temperature	41
6.1.12	Optimum Temperature	42
6.1.13	Land-Surface Temperature	42
6.1.14	Emissivity	43
6.1.15	Normalized Difference Vegetation Index.....	44
6.1.16	Maximum Fraction of Absorbed Photosynthetically Active Radiation	44
6.1.17	Gross Primary Production	45
6.2	Projection.....	45
6.2.1	Grid to Grid.....	46
6.2.2	Swath to Grid.....	46
6.2.3	Grid to Swath	47
6.2.4	Swath to Swath	47
6.3	Model Processing.....	47
6.3.1	Forest Light Environmental Simulator.....	48

6.3.2	Breathing Earth Systems Simulator.....	50
6.3.3	Priestley-Taylor Jet Propulsion Laboratory	53
6.3.4	Water Use Efficiency.....	61
6.3.5	Uncertainty.....	62
7	Dissemination	63
8	Demonstration of Output.....	66
9	Applications.....	69
9.1	Agriculture and Water Rights	69
9.2	Forest and Riparian Management.....	70
10	Conclusion	72
	Bibliography	73

Table of Figures

Figure 1. Late 20 th and early 21 st century global food production (left) and population (right) growth (The World Bank, 2017).....	1
Figure 2. National Interagency Fire Center reports of annual wildfire damage in the United States from 1983 to 2015 (EPA, 2016).....	3
Figure 3. New Mexico Drought Intensity 2000-2017 (United States Drought Monitor, 2017).....	4
Figure 4. Diagram of the water capacity of cool air vs. warm air.....	6
Figure 5. Depiction of the surface energy budget (Langley Advanced Research Center, 2016).....	8
Figure 6. Depiction of the Water Cycle (Goddard Space Flight Center, 2017).....	9
Figure 7. Depiction of the carbon cycle (United States Department of Energy, 2008).....	10
Figure 8. Diagram of stomatal gas exchange (Arizona State University, 2017).....	11
Figure 9. General workflow of the Evapotranspiration Data Pipeline.....	22
Figure 10. MODIS Sinusoidal Tile Grid (Goddard Space Flight Center, 2016).....	24
Figure 11. Elements of an affine transform matrix.....	25
Figure 12. Example of daytime MODIS Terra swaths in one UTC day.....	28
Figure 13. Example of MODIS swaths intersecting a MODIS land tile. In this example, the h08v05 tile intersects three Terra swaths: 1710, 1845, and 1850.....	29
Figure 14. Köppen-Geiger climate classification (Institute for Veterinary Public Health, 2017).....	36
Figure 15. Flowchart of the calculation of albedo from BRDF parameters.....	38
Figure 16. Lookup table of statistical radiative transport from aerosol optical thickness and solar zenith angle.....	39
Figure 17. Four paths of projection.....	46
Figure 18. Flowchart of the Forest Light Environmental Simulator.....	48
Figure 19. Net radiation without using interpolation in FLiES query (left) and net radiation using interpolation in FLiES query (right).....	49
Figure 20. Flowchart of the Breathing Earth Systems Simulator.....	50
Figure 21. Flowchart of PT-JPL partitioning.....	54
Figure 22. Example of WebGIS dissemination system with boxplot queried by hand-drawn region of interest.....	65
Figure 23. Monthly trends of New Mexico evapotranspiration from 2013 to 2015 with interception in blue, transpiration in green, soil evaporation in brown, and total latent heat flux in black.....	66
Figure 24. Eddy covariance measurement of latent heat flux at US-Vcm site compared to New Mexico record of MODIS PT-JPL, including uncertainty.....	67
Figure 25. Scatterplot comparing monthly aggregates of latent heat flux between the US-Vcm eddy covariance site and MODIS PT-JPL.....	67
Figure 26. Time-series of seasonal trends in New Mexico from 2013 to 2015. The first, third, and fifth rows are pseudo-color plots of total latent heat flux at the time of Terra overpass, aggregated by month. The second, fourth, and sixth rows are corresponding false-color plots with soil evaporation in red, canopy transpiration in green, and interception in blue. New Mexico county boundaries are demarcated in white.....	68
Figure 27. Example of high-resolution evapotranspiration imagery for monitoring irrigation in New Mexico.....	70

Table of Tables

Table 1. Summary of retrieved forcing datasets.	32
Table 2. Landsat 8 Operational Land Imager (OLI) and Thermal Infrared Sensor (TIRS) bands (USGS, 2016).	33
Table 3. Constants used in hypsometric equation.	37
Table 4. Quantization factors of FLiES lookup table indices (Ryu, et al., 2011).	49
Table 5. Forcing variables for PT-JPL model.	53

Table of Equations

Equation 1. Formula to calculate day angle from day of year.....	34
Equation 2. Formula to calculate solar declination from day angle.....	34
Equation 3. Sunrise equation for hour angle from latitude and solar declination.....	34
Equation 4. Sunrise hour from sunrise hour angle.....	34
Equation 5. Daylight hours from sunrise hour angle.....	34
Equation 6. Equation for hour angle from hour of day.....	35
Equation 7. Equation for solar zenith angle from solar declination, hour angle, and latitude.....	35
Equation 8. Hypsometric equation for cloud top height from cloud top pressure, surface pressure, and surface temperature.....	37
Equation 9. Formula for blue-sky albedo from white-sky and black-sky albedos.....	39
Equation 10. Albedo from Landsat 8 bands (Yale University, 2017).....	40
Equation 11. Vertical interpolation of atmospheric temperature profiles.....	41
Equation 12. Formula for dew-point temperature from air temperature and relative humidity.....	42
Equation 13. Formula for phenology from net radiation, air temperature, SAVI, and vapor pressure deficit.....	42
Equation 14. Difference in brightness temperature between Landsat 8 band 10 and 11.....	43
Equation 15. Split-window algorithm for LST from Landsat 8 (Jiménez-Muñoz, Sobrino, Skokovic, Mattar, & Cristóbal, 2014).....	43
Equation 16. Leaf Area Index from Normalized Difference Vegetation Index.....	44
Equation 17. Surface emissivity from Leaf Area Index.....	44
Equation 18. NDVI from Landsat 8 bands.....	44
Equation 19. Formula for outgoing shortwave radiation.....	51
Equation 20. Actual water vapor pressure from dew-point temperature.....	51
Equation 21. Formula for clear-sky atmospheric emissivity.....	51
Equation 22. Formula for incoming longwave radiation in clear-sky conditions.....	51
Equation 23. Formula for incoming longwave radiation in cloudy conditions.....	52
Equation 24. Stefan Boltzmann equation for outgoing longwave radiation from land-surface temperature and emissivity.....	52
Equation 25. Formula for net radiation given surface energy balance components.....	52
Equation 26. Sinusoidal integration of instantaneous net radiation across daylight hours for daily average.....	53
Equation 27. Linear conversion of NDVI to SAVI.....	54
Equation 28. Linear conversion of SAVI to fraction of absorbed photosynthetically active radiation.....	55
Equation 29. Fraction of intercepted photosynthetically active radiation from NDVI.....	55
Equation 30. Leaf area index from fraction of intercepted photosynthetically active radiation.....	55
Equation 31. Formula for soil heat flux.....	55
Equation 32. Saturation vapor pressure from air temperature.....	56
Equation 33. Vapor pressure deficit from saturation and actual water vapor pressure.....	56
Equation 34. Relative humidity from actual and saturation water vapor pressure.....	56
Equation 35. Priestley-Taylor slope of the saturation vapor pressure curve from air temperature.....	56
Equation 36. Potential evapotranspiration using Priestley-Taylor without constraints.....	57
Equation 37. Relative surface wetness from relative humidity.....	57
Equation 38. Green canopy fraction as the ratio of absorbed to intercepted photosynthetically active radiation.....	58
Equation 39. Plant temperature constraint from air temperature.....	58
Equation 40. Plant moisture constraint from absorbed photosynthetically active radiation.....	58
Equation 41. Soil moisture constraint from relative humidity and vapor pressure deficit.....	58
Equation 42. Formula to partition net radiation to the soil from total net radiation using leaf area index.....	59
Equation 43. Formula for net radiation to the canopy from total net radiation and net radiation to the soil.....	59

Equation 44. Formula for canopy transpiration, applying relative surface wetness, green canopy fraction, plant temperature and moisture constraints, and net radiation to the canopy to the Priestley-Taylor equation.	59
Equation 45. Formula for interception evaporation, applying relative surface wetness and net radiation to the canopy to the Priestley-Taylor equation.	60
Equation 46. Formula for soil evaporation, applying relative surface wetness, soil moisture constraint, net radiation to the soil, and soil heat flux to the Priestley-Taylor equation.	60
Equation 47. Total instantaneous latent heat flux from sum of partitions.	60
Equation 48. Evaporative Stress Index from latent heat flux and potential evapotranspiration.	61
Equation 49. Evaporative fraction as ratio of latent heat flux to available energy.	61
Equation 50. Daily latent heat flux from evaporative fraction applied to daily integrated net radiation.	61
Equation 51. Daily evapotranspiration in kilograms from daily latent heat flux.	62
Equation 52. Water Use Efficiency as the ratio of gross primary production in grams of carbon to evapotranspiration in kilograms of water.	62

Abstract

Near Real-Time Monitoring of Global Evapotranspiration and its Application to Water Resource Management

By

Gregory H. Halverson

Master of Science in Geographic Information Science

Water scarcity and its impact on agriculture is a pressing world concern. At the heart of this crisis is the balance of water exchange between the land and the atmosphere. The ability to monitor evapotranspiration provides a solution by enabling sustainable irrigation practices. The Priestley-Taylor Jet Propulsion Laboratory model of evapotranspiration has been implemented to meet this need as a daily MODIS product with 1 to 5 km resolution. An automated data pipeline for this model implementation provides daily data with global coverage and near real-time latency. An interactive map providing on-demand statistical analysis enables water resource managers to monitor rates of water loss. To demonstrate the application of remotely-sensed evapotranspiration to water resource management, a partnership has been arranged with the New Mexico Office of the State Engineer (NMOSE). An online water research management tool was developed to meet the specifications of NMOSE using the Leaflet, GeoServer, and Django frameworks. NMOSE will utilize this tool to monitor drought and fire risk and manage irrigation. Through this test-case, it is hoped that real-time, user-friendly remote sensing tools will be adopted globally to make resource management decisions informed by the NASA Earth Observation System.

1 Introduction

Changes in our planet's temperature and precipitation patterns are severely affecting the availability of fresh water in the world, and droughts are becoming more frequent and severe (Ziegler, et al., 2003). This threat to our water security also threatens our food security and other natural resources. This poses administrative challenges for water resource managers as well as rangeland and forest managers. Decisions in water allocation, land use, and fire prevention rely on drought-monitoring data, especially in the realm of agriculture, rangeland management, and forestry. In this fight against drought, floods, fire, and threats to our water, food, and natural resource security, monitoring the evapotranspiration of water from plants and soil is a valuable source of decision-making information and can bring new insight to plant-climate interaction.

Agriculture is the main consumer of water and is severely affected by drought (Morton, 2007). The practice of irrigation makes water a key driver of agricultural production (Hanjra & Qureshi, 2010), which accounts for 70% of the world's water use (Allouche, 2011).

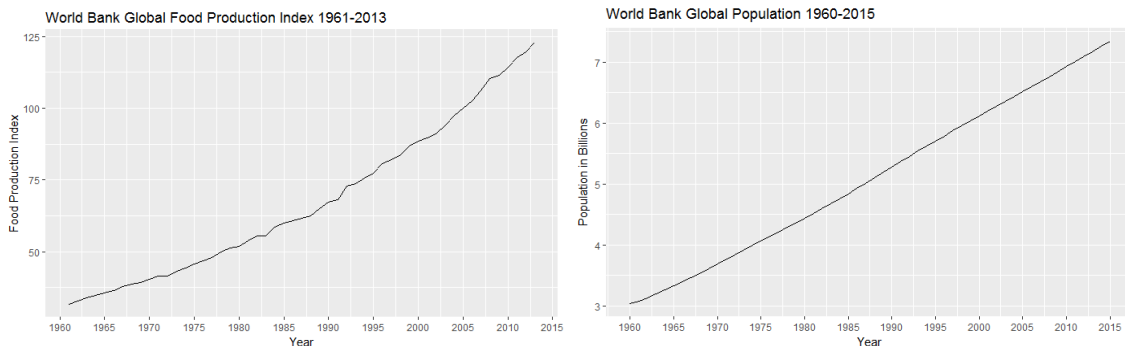


Figure 1. Late 20th and early 21st century global food production (left) and population (right) growth (The World Bank, 2017).

Over the past half century, global food production has been increasing each year by 2.7% (Figure 1) (The World Bank, 2017), and global population has increased 1.6% per year (Figure 1) (The World Bank, 2017). Agricultural productivity must continue to increase to feed this growing population. The Intergovernmental Panel on Climate Change estimates that a global population of 9 billion by 2050 will require a 60% increase in food production (IPCC, 2014), increasing agricultural demand for water. This continued increase in food production will require monitoring agricultural water use in the form of evapotranspiration from crops and crop lands.

Up to two billion people in this growing population depend on the food provided by rangelands, as these lands encompass up to 40% of the Earth's surface (Sayre, McAllister, Bestelmeyer, Moritz, & Turner, 2013). Prior to extensive land use change, rangelands, including grasslands, shrub lands, savannahs, and tundra, covered more than half of the land-surface and supported more than half of world livestock (Biazin & Sterk, 2012). The challenges associated with managing these diminishing rangelands include responding to an increasing intensity of drought, higher temperatures, and changing precipitation patterns (Breshears, Knapp, Law, Smith, & Twidwell, 2016). Warmer temperatures increase atmospheric demand for water and soil evaporation rates, leaving less water for plants and increasing plant stress (Breshears, Knapp, Law, Smith, & Twidwell, 2016). The dry, bare soil left behind by drought is vulnerable to wind erosion as well as erosion from flooding after periods of drought (Breshears, Knapp, Law, Smith, & Twidwell, 2016). This risk of degradation and aridification in the world's rangelands due to drought further threaten the world's food supply in addition to the threat faced by agriculture. Preventing and reversing loss of rangelands will require monitoring of the aridification and recovery process in the form of evapotranspiration from rangeland flora and soil.

This risk of aridification leads to an elevated risk of wildfire. Not only rangelands are vulnerable to fire, but drying forests and other ecosystems present a major fire risk as well. This risk was highlighted in 2016 by a massive tree die-off in California (Chow, 2016) and a mega-fire in Appalachia (Boddy, 2016). Hundreds of homes are burned annually by wildfire (Westerling, Hidalgo, Cayan, & Swetnam, 2006). Wildfire damage in the United States has been trending upward and increased over 6 and a half times from 1983 to 2015 (Figure 2) (EPA, 2016). Prevention and containment of wildfires will require continual evaluation of the spatial distribution of fire risk in forests and rangelands due to dry trees and shrubs as indicated through monitoring of evapotranspiration.

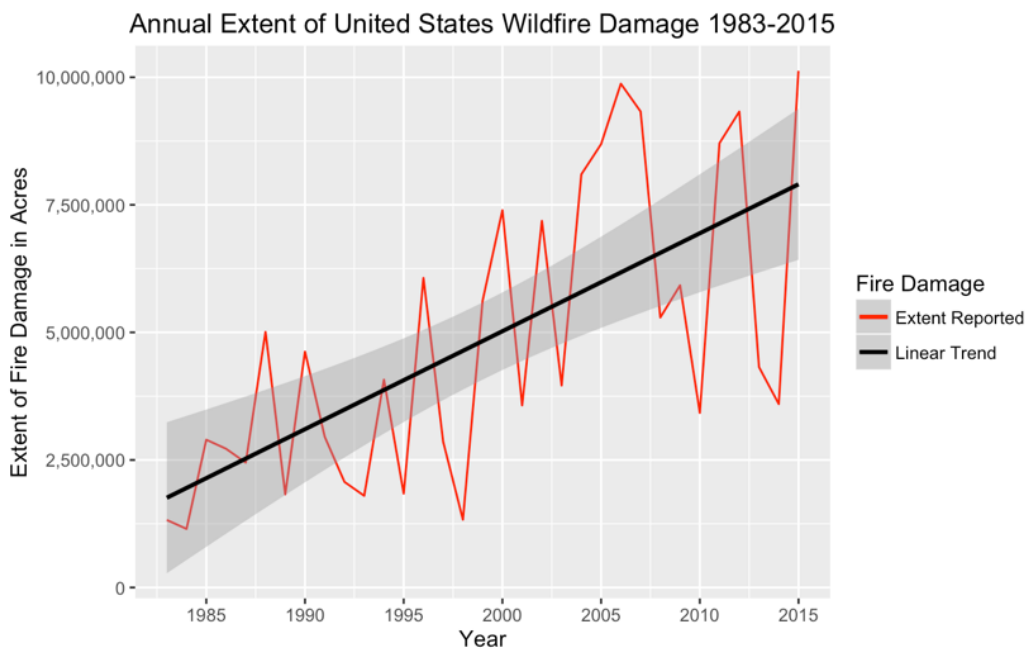


Figure 2. National Interagency Fire Center reports of annual wildfire damage in the United States from 1983 to 2015 (EPA, 2016).

A potential mitigation of these problems in the human-environment interaction is to monitor fluctuations in water. The solution proposed here to solve this problem is to use remote sensing data to calculate rates of evapotranspiration at both high spatial and temporal resolution and provide near real-time, interactive maps of these data to water

resource managers, rangeland managers, and forest managers. The evapotranspiration monitoring system demonstrated here, the Evapotranspiration Data Pipeline, will automate processing and dissemination of evapotranspiration data based on observations from the Moderate Resolution Imaging Spectroradiometer (MODIS) using the Priestley-Taylor Jet Propulsion Laboratory model of evapotranspiration.

1.1 Partnership with the New Mexico Office of the State Engineer

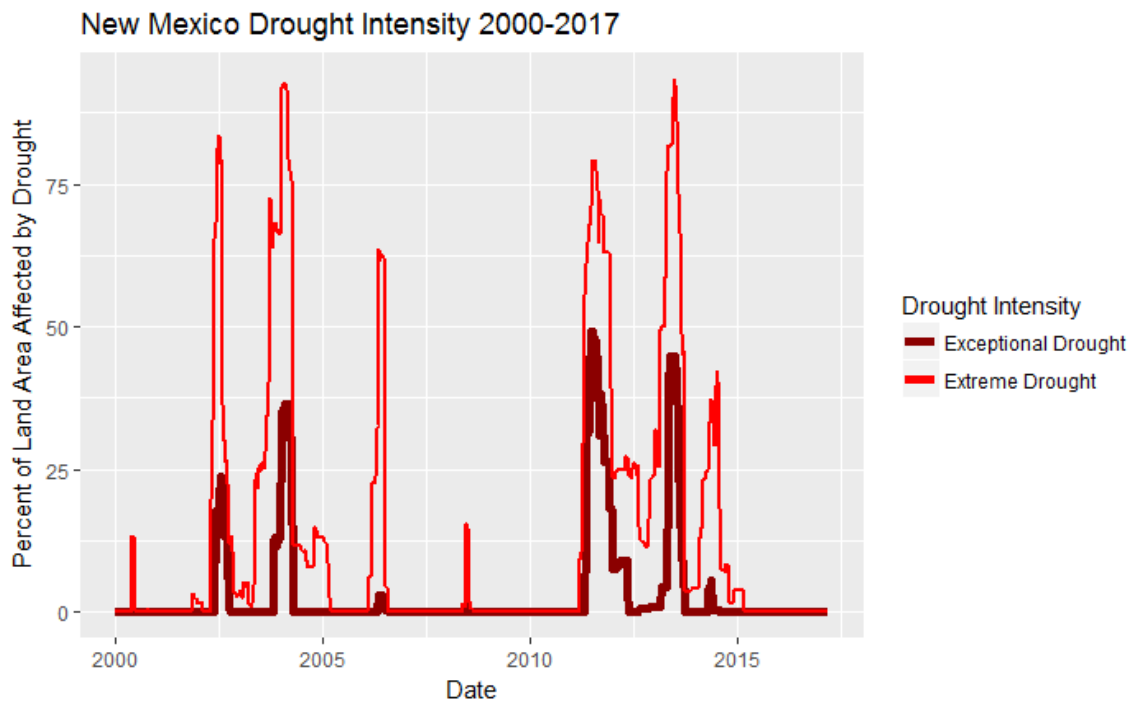


Figure 3. New Mexico Drought Intensity 2000-2017 (United States Drought Monitor, 2017).

The State of New Mexico has been affected by several periods of severe drought in the 21st century, with a US Drought Monitor assessment of Exceptional Drought reaching up to half of the state and Extreme Drought affecting over 75% of the state’s land area (Figure 3) (United States Drought Monitor, 2017). To apply the Evapotranspiration Data Pipeline to agricultural water management, a partnership has been formed with the New Mexico Office of the State Engineer (NMOSE). The goal of this partnership is to provide the State

of New Mexico with an operational system to enhance water security and characterize water demand vs. supply to improve decision making. An online water research management tool was developed to meet the specifications of NMOSE using the Leaflet, GeoServer, and Django frameworks. NMOSE will utilize this tool to monitor drought and fire risk and manage irrigation. Through this test-case, it is hoped that real-time, user-friendly remote sensing tools will be adopted globally to make resource management decisions informed by the NASA Earth Observation System.

1.2 Collaboration with the ECOSTRESS Mission

The methods described in this document to produce the MODIS 1 km PT-JPL and Landsat 30m PT-JPL data products are also being developed and tested in collaboration with the Ecosystem Spaceborne Thermal Radiometer Experiment on Space Station (ECOSTRESS) mission to produce an ECOSTRESS evapotranspiration product as well, using diurnal land-surface temperature. This high-resolution, diurnal evapotranspiration product will facilitate smaller scale agricultural management and precision agriculture as well as reveal new insight into stomatal function and plant-climate interaction over the course of the day.

2 Background

This section explains the broad overview of the physical geography represented in this model, including the role the evapotranspiration process plays in land-atmosphere interaction and the natural cycles of energy, water, and carbon.

2.1 Evapotranspiration

Evapotranspiration (ET) is the transfer of water from the land to the atmosphere (Fisher, 2012). Evapotranspiration is determined by the water capacity of the air and the energy available to break the bonds of water molecules.

2.2 Water Capacity of the Air

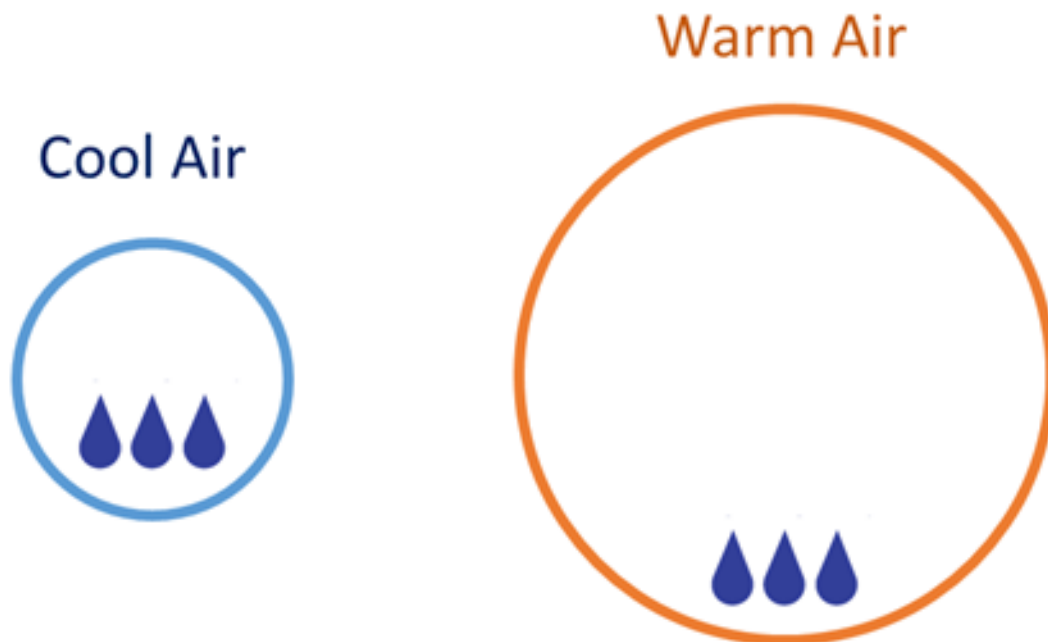


Figure 4. Diagram of the water capacity of cool air vs. warm air.

The water capacity of the air is determined by air temperature. Cool air can hold less water vapor, and warm air can hold more water vapor (Figure 4). When the air is full of water vapor, this vapor condenses at the same rate that it evaporates. This equilibrium is called

saturation. The maximum limit of water in the air can be determined from air temperature as saturation vapor pressure. The temperature which air would have to be to reach saturation and condense its water vapor into dew is called the dew-point temperature, which corresponds to the actual level of vapor pressure in the air. The ratio of actual vapor pressure to saturation vapor pressure is expressed as a proportion called relative humidity. The difference of saturation vapor pressure and actual vapor pressure is called vapor pressure deficit. This deficit determines the potential for the air to absorb water from evapotranspiration.

2.3 Cycles of the Land Surface

There are three cycles of the terrestrial surface surrounding evapotranspiration: the surface energy balance, the water cycle, and the carbon cycle. The models implemented in this thesis consider only the land surface because sea-surface temperature cannot be modeled the same way as land-surface temperature, and the evaporation of the ocean and bodies of water is a fundamentally separate process from that of the evaporation of soil moisture and transpiration of water from plants.

2.3.1 Surface Energy Budget

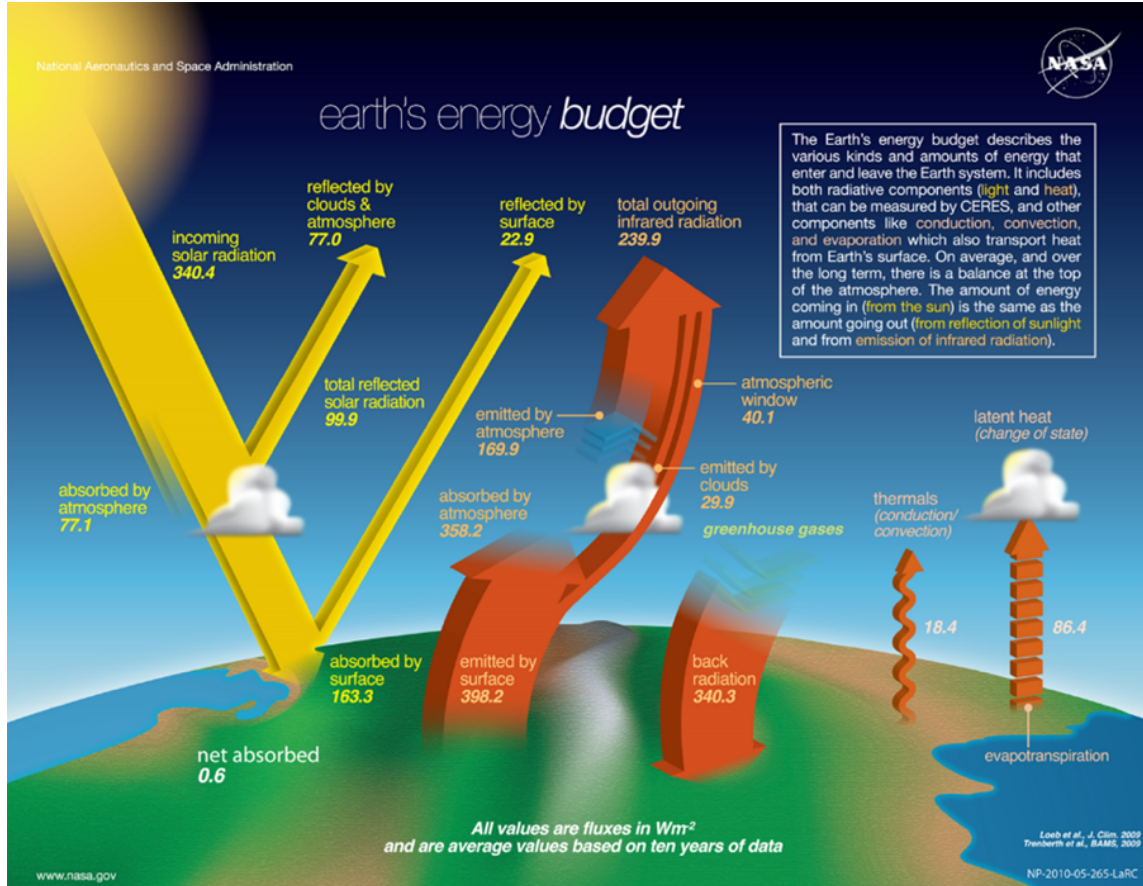


Figure 5. Depiction of the surface energy budget (Langley Advanced Research Center, 2016).

The surface energy budget describes the interactions of energy entering and leaving the surface of the Earth (Figure 5) (Langley Advanced Research Center, 2016). The largest source of energy in the evapotranspiration process is solar radiation (Allen, Pereira, Raes, & Smith, 2006). Incoming shortwave radiation is a measure of the sunlight hitting the surface of the Earth. It is attenuated depending on the transmissivity of the atmosphere and is reflected from the Earth's surface depending on albedo. Incoming longwave radiation is emitted to the surface by greenhouse gases. And outgoing longwave radiation is the energy emitted out from the Earth's surface, which we can measure from space as land-surface temperature and emissivity. Together, the total energy budget left over at the Earth's surface is called net radiation. This remaining energy, can be absorbed in three main ways:

transfer into the air as sensible heat flux, transfer into the ground as soil heat flux, and transfer into water as latent heat flux. Latent heat flux is evapotranspiration measured as a rate of energy exchange.

2.3.2 Water Cycle

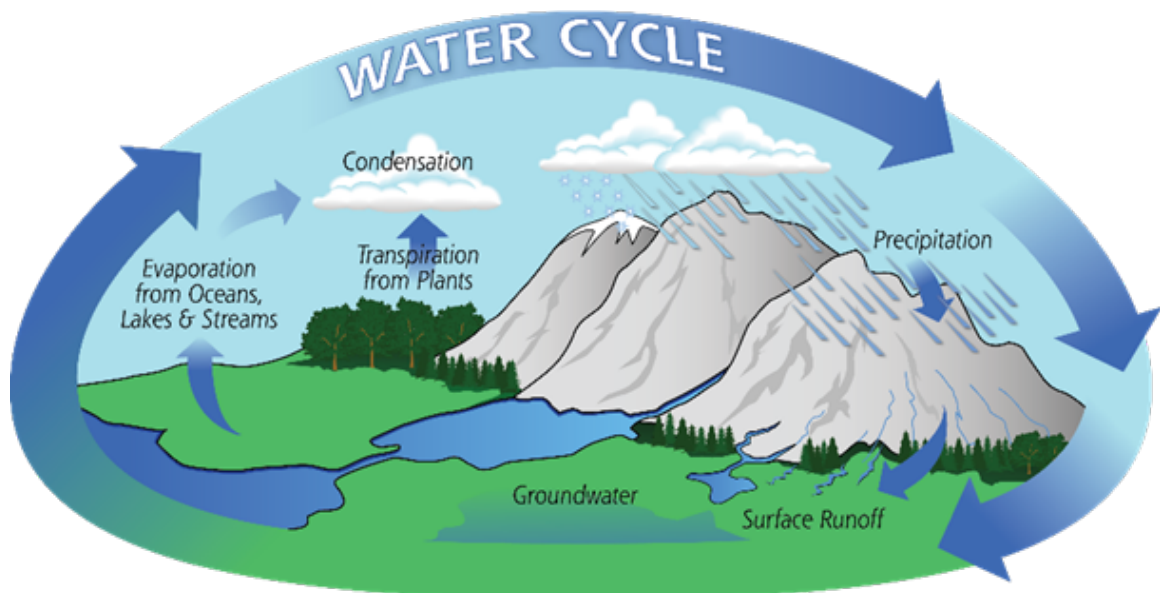


Figure 6. Depiction of the Water Cycle (Goddard Space Flight Center, 2017).

Evapotranspiration is a key variable in the water cycle (Figure 6) (Goddard Space Flight Center, 2017), and its measurement is an excellent indicator of the intensity of the water cycle (Huntington, 2005), including the risk of drought and flood. In the lower portion of the Earth's atmosphere, the troposphere, air temperature decreases with elevation. When water vapor rises to the cold air higher in the troposphere, it condenses to form clouds and release precipitation, the incoming source of fresh water on the land. This precipitation moistens the soil and may infiltrate the land surface to recharge ground water, or it may discharge as runoff through streams and rivers into bodies of water. It may be intercepted or absorbed by plants. When water circulating through plants evaporates due to latent heat flux, it causes pores in the plants called stomata to open and release water vapor as transpiration. Water intercepted on the tops of leaves and water moistening the soil may

also evaporate. These combined sources of water vapor form evapotranspiration and complete the cycle.

2.3.3 Carbon Cycle

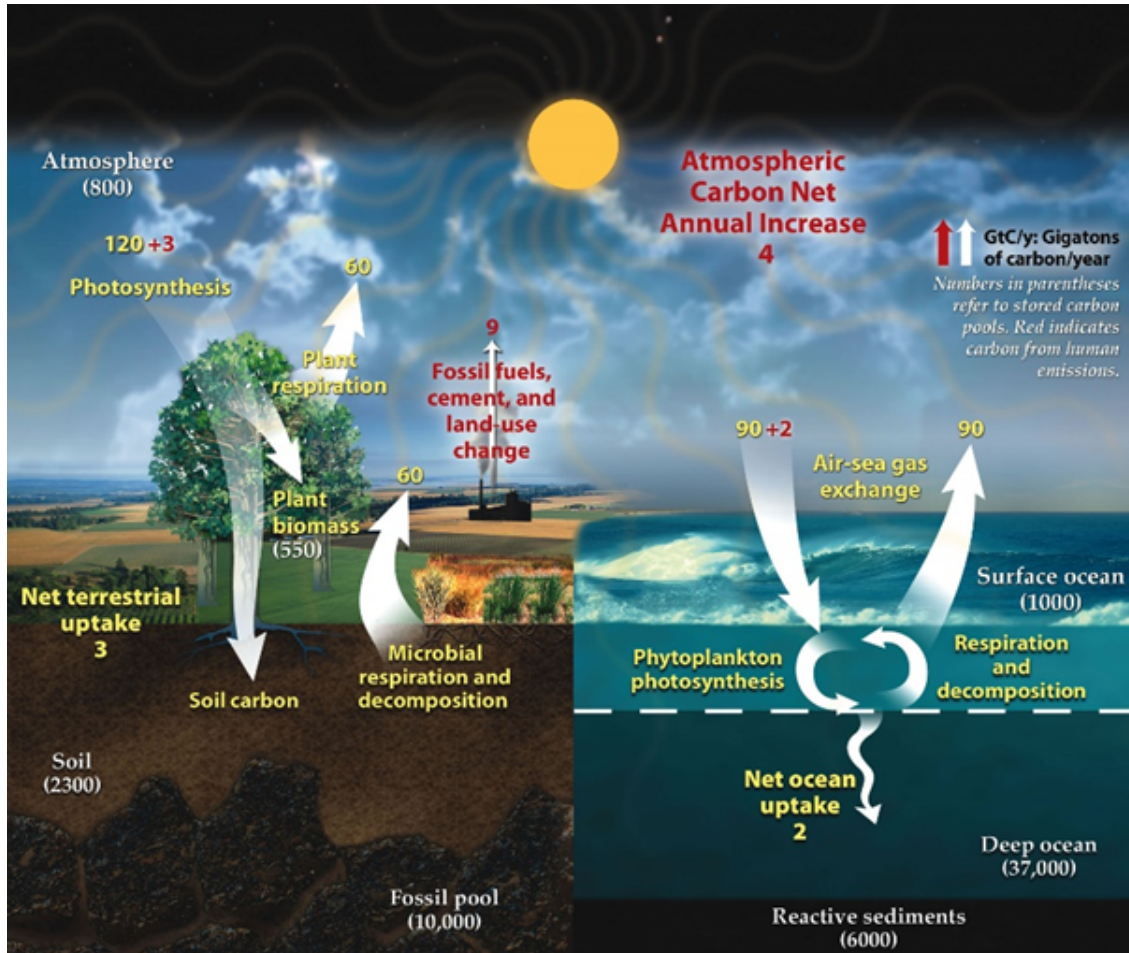


Figure 7. Depiction of the carbon cycle (United States Department of Energy, 2008).

Evapotranspiration has a strong influence on photosynthesis, a key variable in the carbon cycle (Figure 7) (United States Department of Energy, 2008). Photosynthetic organisms, such as plants, absorb carbon dioxide and water. Solar radiation excites the conversion of carbon dioxide and water into sugars that are used to form adenosine triphosphate (ATP). This process is called photosynthesis, and it is measured as gross primary productivity (GPP). The ratio of GPP to ET is called Water Use Efficiency (WUE) (Mu, Zhao, & Running, 2011).

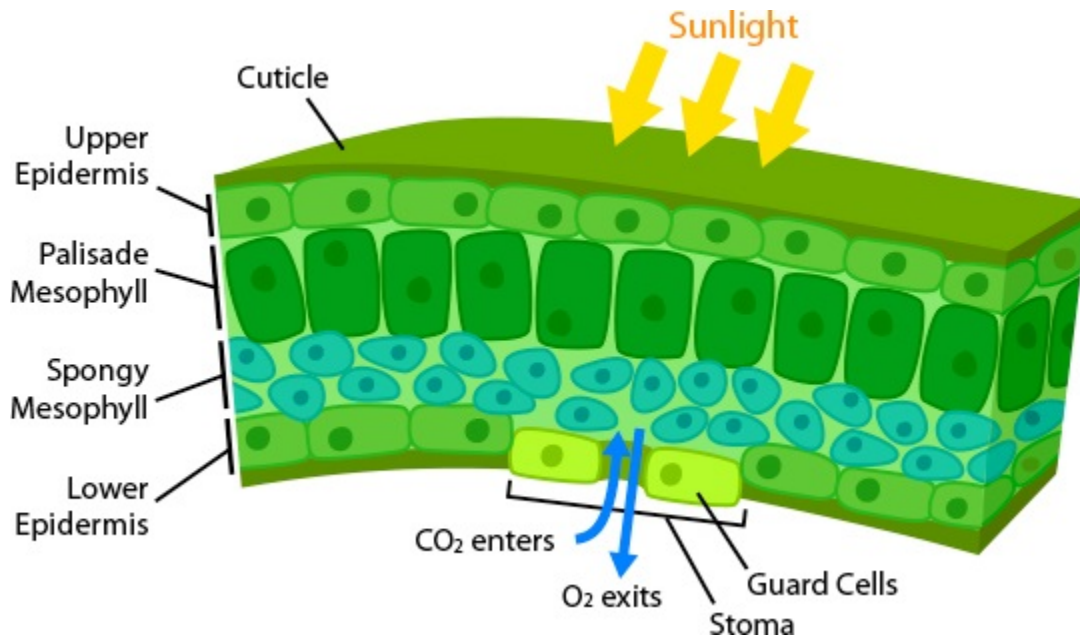


Figure 8. Diagram of stomatal gas exchange (Arizona State University, 2017).

Plants absorb carbon dioxide through their stomata (Figure 8) (Arizona State University, 2017) when they are open due to transpiration. When plants are water-stressed, they close their stomata to conserve water. This desperate act restricts the gas exchange that allows plants to absorb carbon dioxide and photosynthesize. And so, interruptions to the supply of fresh water needed by plants leads to carbon-starvation and ultimately death. This causes crop failure that adds to world hunger and increases the concentration of carbon dioxide in the atmosphere that produces incoming longwave radiation.

3 Literature Review

This section reviews the precedents established in both creating an operational automated system to provide near real-time land-surface conditions for natural resources management as well as methodological approaches established in the remote sensing of evapotranspiration.

3.1 Examples of Operational Water Monitoring Systems

The systems described here establish the precedent for creating an operational drought-monitoring system to improve global agriculture.

3.1.1 GLAM

The Global Agricultural Monitoring Project (GLAM) is a joint National Aeronautics and Space Administration (NASA), United States Department of Agriculture (USDA), University of Maryland, Duluth (UMD), and San Diego State University (SDSU) initiative (Becker-Reshef, et al., 2010). GLAM is a global agricultural monitoring system that provides timely, accessible, and validated remote sensing products and analysis tools for crop monitoring and assessment. This system is utilized in the USDA Foreign Agricultural Service (FAS) Decision Support System (DSS).

Agricultural production is strained socially by the poverty and conflict of global population growth and ecologically by changes in precipitation. Maintaining global food security requires global agricultural intelligence. The USDA FAS is the only agency responding to these concerns with global crop production forecasts using GLAM.

A customized GIS system, including data archiving, processing, and delivery systems was developed to meet the needs of the FAS analysts. This system re-projects and composites

MODIS vegetation indices to a specified region of interest. A web interface allows FAS analysts to better monitor land surface conditions at the pixel level.

Data delivery timeliness is the key requirement for an effective agricultural monitoring system. MODIS provides near real-time, global, daily corrected-reflectance imagery, with fast turnaround, 2 to 4 hours after acquisition.

The USDA FAS has contributed new products and methods of analysis in their global system. GLAM has developed a cumulative vegetation index (CVI), which is the sum of NDVI from the start of the growing season to the present. This enhanced vegetation index improves monitoring of crops over the growing season. The USDA FAS Global Reservoir and Lake Monitor (GRLM) records variations in many water bodies worldwide using satellite radar altimetry.

This system is being internationalized into a global cooperative through the Group on Earth Observations (GEO) organization. Validation of this system is provided with the Production Acreage and Yield (PAY) database. PAY identifies the level of disagreement between crop statistics generated by international agencies.

The need for global agricultural monitoring using the Earth Observation System will continue to grow due to the increasing frequency of extreme climate events including floods and drought. Population growth, economic growth, and energy demands also continue to increase the need for operational global systems.

The disadvantage to GLAM is that it is an NDVI-based system. The PT-JPL system provides much finer ecological detail in its assessment of crop health, taking both land-surface and atmospheric conditions into account in the calculation of evapotranspiration.

3.1.2 GIDMaPS

The Global Integrated Drought Monitoring and Prediction System (GIDMaPS) is a near real-time monitoring and seasonal prediction system for multiple drought indicators (Hao, AghaKouchak, Nakhjiri, & Farahmand, 2014). The GIDMaPS system provides meteorological and agricultural drought information based on multiple drought indicators.

The GIDMaPS system relies on reanalysis data as its input. A reanalysis is a data assimilation project that applies a consistent assimilation scheme to historical observations spanning an extended period. GIDMaPS uses precipitation and soil moisture data from the Modern Era Retrospective analysis for Research and Applications (MERRA-Land), North American Land Data Assimilation System (NLDAS), Global Land Data Assimilation System (GLDAS), and the Global Drought Climate Data Record (GDCCR).

Three drought monitoring indexes are collected from these reanalysis products: the Standardized Precipitation Index (SPI), the Standardized Soil Moisture Index (SSI), and the Multivariate Standardized Drought Index (MSDI). The historic record of these indices is extrapolated into forecasts, and the ensemble median of these forecasts is standardized and published as a drought severity indicator.

The advantage to using GIDMaPS is its forecasting ability and its inclusion of precipitation and soil moisture. Its disadvantage is that it relies entirely on coarse spatial resolution reanalysis data. In contrast, the PT-JPL system primarily uses high resolution satellite imagery that can be used for precision analysis and decision making.

3.2 Approaches to Remote Sensing of Evapotranspiration

Remote sensing of evapotranspiration generally involves satellite imaging of land-surface temperature, vegetation index, and albedo. Various algorithms have been developed to

calculate the surface energy budget from these variables. Some algorithms also incorporate meteorological data, which can also be remotely sensed.

Calculation of evapotranspiration in the surface energy budget requires partitioning net radiation into soil heat flux, sensible heat flux, and latent heat flux. Soil heat flux is the energy utilized in heating the soil. Sensible heat flux is the rate of heat loss of the surface to the air through convection and conduction due to the difference in surface and air temperature. Latent heat flux is the rate of heat loss from the surface due to evapotranspiration.

A variety of surface energy balance models have been developed for partitioning net radiation into these components. This brief history explains the development from simple NDVI and LST based drought indices to the PT-JPL model used in the Evapotranspiration Data Pipeline.

3.2.1 SEBS

The Surface Energy Balance Index (SEBI), is based on the Crop Water Stress Index (CWSI) and derives evapotranspiration from the contrast between wet and dry regions (Liou & Kar, 2014). SEBI scales surface temperature in a maximum range of surface temperature and the upper and lower bounds of the surface and air temperature difference.

The Surface Energy Balance System (SEBS), estimates the surface energy balance from remotely sensed data using a modified form of SEBI (Liou & Kar, 2014). SEBS calculates the physical parameters of the land surface, roughness length for heat transfer, and evaporative fraction based on energy balance at limiting cases. In dry conditions, latent heat flux approaches zero and sensible heat flux reaches maximum. In wet conditions, evapotranspiration reaches its potential and sensible heat flux reaches its minimum. The

limiting cases of SEBS minimize the uncertainty in surface temperature and meteorology. Other advantages of the SEBS model include formulation of variable roughness height for heat transfer, characterizing turbulent heat fluxes without prior knowledge, and representativeness of surface resistance parameters.

3.2.2 METRIC

The Surface Energy Balance Algorithm for Land (SEBAL) is an image-processing model for calculating evapotranspiration as the residual of the surface energy balance (Liou & Kar, 2014). SEBAL uses empirical relationships and physical parameterization with satellite imagery of visible, near infra-red, thermal infrared radiation, surface temperature, NDVI, and albedo.

The Mapping Evapotranspiration at High Resolution and with Internalized Calibration (METRIC) model, by Dr. Rick Allen, is a variant of SEBAL (Liou & Kar, 2014). METRIC extends SEBAL by integrating reference ET using ground-based wind speed and near-surface dew point temperature. Anchor conditions are selected within an observed scene to internally calibrate sensible and latent heat flux and avoid the need to apply a radiative transfer model for atmospheric correction of surface temperature and albedo.

3.2.3 ALEXI

Dr. Martha Anderson of the United States Department of Agriculture specializes in the application of remotely sensed thermal infra-red (TIR) imaging to detect agricultural water stress. Her model of evapotranspiration, the Atmosphere Land Exchange Inverse (ALEXI) model, is a two-source model that combines the two-source energy balance (TSEB) model with an atmospheric boundary layer (ABL) model (Anderson, et al., 2011). Two source

approaches such as this partition the surface energy budget into soil and canopy components (Liou & Kar, 2014).

Net radiation is partitioned into soil and canopy components. Detection of plant water stress through calculation of transpiration is accomplished by applying the Priestley-Taylor model to the canopy component of net radiation. The rate of soil evaporation is calculated as the residual of the surface energy budget.

The DisALEXI extension to the ALEXI model spatially disaggregates ALEXI estimates of surface energy fluxes to higher resolutions. Following the DisTrad method (Kustas, Norman, Anderson, & French, 2003), DisALEXI spatially sharpens land-surface temperature (LST) using high-resolution normalized difference vegetation index (NDVI). Dr. Anderson notes though, that the fundamental flaw of using the LST-NDVI relationship to downscale LST results in an over-enhancement in the contrast of the LST that does not detect changes in water in real time, because the variability of NDVI only relates the long-term growth and health of plants, not immediate changes in water.

Dr. Anderson also makes use of the frequent availability of low-resolution remote sensing imagery combined with the infrequent availability of high-resolution imagery using the Spatial Temporal Adaptive Reflectance Fusion Model (STARFM) (Gao, Masek, Schwaller, & Hall, 2006). By applying DisALEXI to both high-temporal, low-spatial resolution MODIS and low-temporal, high-spatial resolution Landsat, these maps can be combined into a high-temporal, high-spatial resolution time-series using STARFM.

3.2.4 BESS

Most remote sensing models of evapotranspiration focus on estimations of surface energy balance from remotely sensed land conditions and rely on sparse meteorological data

obtained from weather stations or spatially coarse reanalysis datasets. Dr. Youngryel Ryu demonstrated methods of overcoming this by utilizing the atmospheric imaging capabilities of MODIS in addition to its land monitoring capabilities, enabling the development of a global MODIS evapotranspiration product (Ryu, et al., 2011). His proposal to synthesize MODIS land and atmosphere products to compute GPP (2.3.3) and evapotranspiration (ET) is called the Breathing Earth Systems Simulator (BESS). BESS is a process based model that does not rely on internal calibration like METRIC.

A contributing author to BESS, Dr. Hideki Kobayashi, developed a radiative transfer model called the Forest Light Environmental Simulator (FLiES) (Kobayashi & Iwabuchi, 2008). BESS utilizes this model to calculate incoming shortwave radiation from aerosol optical thickness, cloud optical thickness, land surface albedo, cloud top height, atmospheric profile type, aerosol type, and cloud type.

A quadratic form of the Penman-Monteith equation is used to calculate two-leaf latent heat flux. A second order Taylor expansion is used to estimate saturated vapor pressure at the leaf surface from air temperature. The quadratic form of the Penman-Monteith equation uses the same inputs as the conventional Penman-Monteith: aerodynamic resistance, air density, psychrometric constant, saturated vapor pressure, and net radiation.

Because of its process-based algorithm that does not require the type of supervised calibration or internal calibration that SEBAL and METRIC do, BESS is a prime candidate for operational remote sensing of net radiation on a global scale. The Evapotranspiration Data Pipeline incorporates a variant of the BESS model to calculate net radiation (6.3.2). The quadratic Penman-Monteith model used to process net radiation into

evapotranspiration is not followed in the Evapotranspiration Data Pipeline and is instead replaced by the Priestley-Taylor Jet Propulsion Laboratory model (6.3.3).

3.2.5 PT-JPL

Dr. Joshua Fisher explores the use of the Priestley-Taylor equation in the global modeling of evapotranspiration (Fisher, Tu, & Baldocchi, Global estimates of the land-atmosphere water flux based on monthly AVHRR and ISLSCP-II data, validated at 16 FLUXNET sites, 2008). Penman-Monteith is the most theoretically accurate model of evapotranspiration, but it is a challenge to deploy globally because it depends on measurements of aerodynamic resistance, stomatal resistance, and wind speed. The Priestley-Taylor equation is a simplification of the Penman-Monteith model that replaces the more complicated parts of the equation with the Priestley-Taylor coefficient, which can be assumed constant.

By holding the Priestley-Taylor coefficient constant, potential evapotranspiration can be calculated. The Priestley-Taylor Jet Propulsion Laboratory (PT-JPL) model extends this model to scale estimates of potential evapotranspiration to actual transpiration using remotely sensed surface meteorological data. PT-JPL partitions latent heat flux (LE) into three components: canopy transpiration, soil evaporation, and interception evaporation. Canopy transpiration is the amount of latent energy released as water vapor from the stomata of plants. Soil evaporation is the loss of soil moisture. And interception evaporation is the evaporation of dew from the surface of plants. Each of these three LE components are calculated separately using modifications of the Priestley-Taylor equation that incorporate eco-physiological constraint factors. These constraint factors include relative surface wetness, green canopy fraction, plant temperature constraint, plant moisture constraint, and soil moisture constraint.

Relative surface wetness is calculated as the fourth power of relative humidity. Green canopy fraction is calculated as the ratio of the fraction of photosynthetically active radiation (PAR) absorbed by green vegetation cover (fAPAR) to the fraction of PAR intercepted by total vegetation cover (fIPAR). Plant temperature constraint is calculated from difference of maximum temperature and optimum temperature. And soil moisture constraint is calculated from relative humidity raised to a constant fraction of vapor pressure deficit. Canopy transpiration constrains Priestley-Taylor using relative surface wetness, green canopy fraction, plant temperature constraint, and plant moisture constraint. Soil evaporation uses relative surface wetness and soil moisture constraint. Interception evaporation uses only relative surface wetness.

Net radiation is partitioned into net radiation to the soil and net radiation to the canopy. The vegetative components of the LE partition, canopy transpiration and interception evaporation, use canopy net radiation as the radiative parameter of the Priestley-Taylor equation. The soil evaporation component uses the difference between net radiation to the soil and soil heat flux as the radiative parameter.

The advantage of PT-JPL against SEBAL and METRIC is that it requires no site calibration or tuning and can be applied on a per-pixel basis. While many other surface energy balance partitioning models rely on the regional statistical relationships between variables that can be extracted on a scene-by-scene basis with remote sensing data, PT-JPL is independent and abstract, capable of performing calculations both on *in situ* point data and on remotely sensed rasters of any extent, including global.

The ability to arbitrarily segment global raster data for processing makes this model a prime candidate for supercomputing using embarrassingly parallel processes. PT-JPL forms the

core methodology of the Evapotranspiration Data Pipeline (6.3.3) as an operational algorithm capable of producing a global evapotranspiration remote sensing product.

The PT-JPL model has been repeatedly and independently validated. An evaluation of PT-JPL, SEBS, and MOD16 against flux tower observations found that PT-JPL had the highest Kendall's tau, lowest RMSD, and smallest bias (Vinukollu, Wood, Ferguson, & Fisher, 2010). A global comparison of several models found that PT-JPL evapotranspiration provided the highest statistical measures of agreement with flux tower observations and is a reliable model over a range of land surface conditions (Ershadi, McCabe, Evans, Chaney, & Wood, 2014). And a regional evaluation of several models over China found PT-JPL to have the highest coefficient of determination compared to flux tower observations (Chen, et al., 2014). In each study, PT-JPL was demonstrated to have the highest performance in predicting ground observations of evapotranspiration.

4 Processing Overview

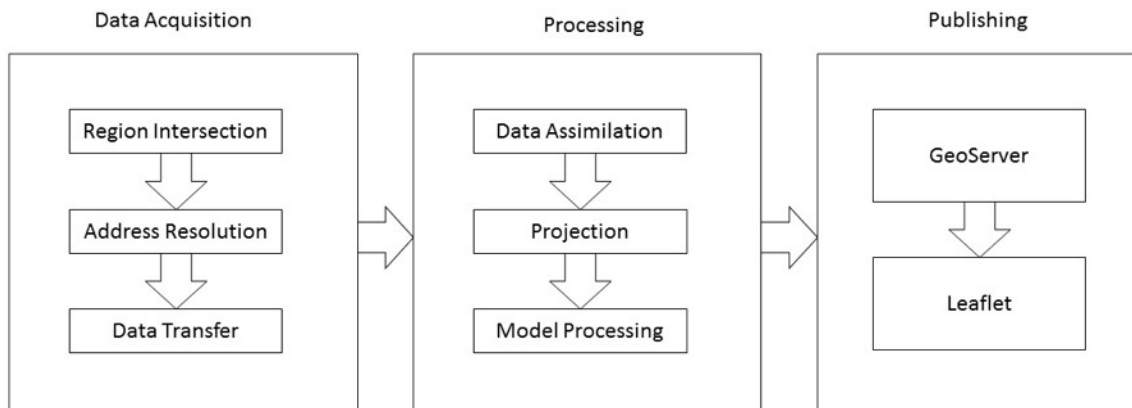


Figure 9. General workflow of the Evapotranspiration Data Pipeline.

The Evapotranspiration Data Pipeline coordinates a sequence of operations to obtain, process, and disseminate evapotranspiration data (Figure 9). Data is acquired by determining which scenes of source data are appropriate for a target time and spatial extent, resolving remote addresses for these scenes, and transferring them to local storage. Data is processed by preprocessing these source data products into a consistent form and projecting them into the target extent, then ingesting these forcing data variables in a sequence of environmental models. The spatially discrete nature of the PT-JPL model allows this process to run on an arbitrary spatial extent, which allows this processing pipeline to concurrently process this data product for many target regions of interest as embarrassingly parallel processes. When a global map of these products has been mosaicked together, it is published to resource managers using a WebGIS system.

5 Data Acquisition

The pipeline acquires data in three steps (Figure 9). First, the pipeline needs to know which regions of source data spatially and temporally intersect the target region. These required scenes are then resolved to remote addresses. These remote scenes are transferred to the local filesystem.

5.1 Region Intersection

Remote sensing and reanalysis data come in a diversity of projections, resolutions, and extents. Efficient acquisition of source data for a given processing region requires calculation of which source regions intersect with a given region of interest. This selection of source scenes is determined by calculating the boundary polygons of source and target regions, transforming them to geographic coordinates, and intersecting these polygons.

5.1.1 MODIS Land Tiles

MODIS land data are organized into tiled regions using the Sinusoidal Tile Grid. This tiling system is preserved as the basic spatial unit of processing for PT-JPL as a higher-level MODIS land data product.

5.1.1.1 Sinusoidal Tile Grid

The Sinusoidal Tile Grid projects the Earth's surface onto a Cartesian plane in meters using sinusoidal projection. This plane is divided into a tile grid with 18 rows and 36 columns referenced using zero-based indexing (Figure 10) (Goddard Space Flight Center, 2016). The naming convention for these tiles is the letter h, two-digit horizontal index, the letter v, and two-digit vertical index, such as "h08v05" for the tile covering California. Using 36 columns to divide 360 degrees of longitude makes the width of the tiles equivalent to 10 degrees at the equator. This geographic width tapers at extreme latitudes. The advantages

of using this projection include minimizing distortion of area and facilitating global means without using latitudinal weighting.

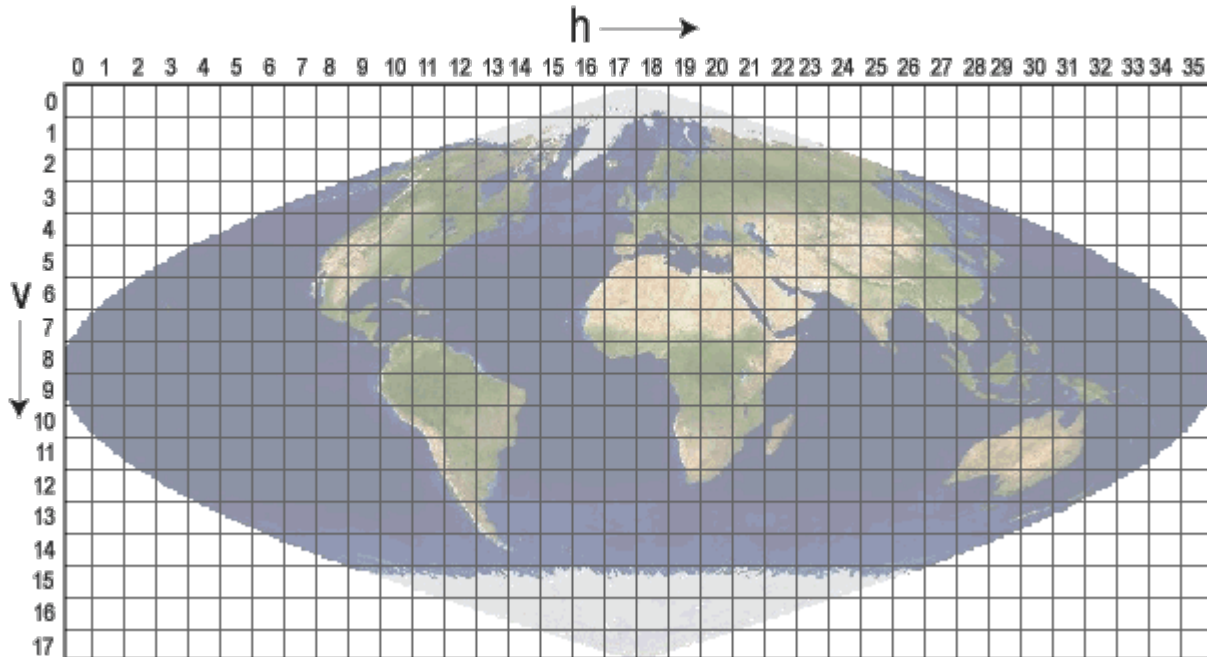


Figure 10. MODIS Sinusoidal Tile Grid (Goddard Space Flight Center, 2016).

These tiles are square, with a constant width and height of 1,111,950.52 meters. The Cartesian plane of this projection has its origin centered on the map, and the corners of this plane extend into non-geographic space 20,015,109.36 meters in the x dimension and 10,007,554.68 meters in the y dimension.

The bounding boxes of these tiles are determined by multiplying the tile width constant by horizontal and vertical indices and offsetting this distance from the upper left extreme of the plane. The boundary polygons defining these regions for intersection are constructed from the corner coordinates of these bounding boxes transformed into geographic coordinates using the *pyproj* library.

5.1.1.2 Affine Transform

Cell Width	Row Rotation	X Origin
Column Rotation	Cell Height	Y Origin
0	0	1

Figure 11. Elements of an affine transform matrix.

The advantage of using projected rasters is that the coordinate of any cell can quickly be calculated using an affine transform. An affine transform is a matrix that includes the x and y coordinates of the top left corner of the top left cell of a raster as well as a positive cell width and negative cell height. Multiplying a pair of array indices by this transform produces a pair of projected coordinates. The *affine* and *NumPy* libraries are used together in python to produce geolocation arrays of MODIS sinusoidal tiles very quickly using affine transforms.

5.1.2 MODIS Swaths

MODIS atmospheric data products are not projected and retain the original geolocation of sensor readings from the satellite. A swath is a section of satellite orbit. While projected rasters are formed from a grid of coordinates at even intervals, swath rasters are dimensioned by the along-track movement of the satellite's position and the cross-track sampling of sensor readings. The coordinates of these sensor readings are given as matrices of latitude and longitude dimensioned by the same along-track and cross-track intervals. The geolocation of these swath data does not conform to any projection and cannot be georeferenced using an affine transform.

The MODIS sensor demarcates its swaths in intervals of 5 minutes of orbit of the Terra or Aqua satellite starting at midnight UTC. These 5-minute intervals equate to 10 km of

change in swath ground track position along the Earth's surface at nadir. The cross-track swath width of the MODIS sensor's field of view projected to the Earth's surface is 2,330 km.

In the predecessor to the system described here, MODIS atmospheric data was instead obtained in MODIS land tile format from the Lawrence Berkeley National Laboratory (LBNL), which did not require this region matching and projection system to operate. This LBNL data was only available until 2009. The system described in this document was developed as a response to this limitation in order to support the inclusion of ECOSTRESS and the production of MODIS PT-JPL from 2010 onwards.

5.1.2.1 Swath Ground Track Orbital Calculation

Calculating the boundary of a swath requires calculating a series of satellite positions including at least the beginning and end of the swath ground track. The temporal resolution of this swath ground track calculation can be increased with the number of points calculated along the swath ground track, dividing the swath's flight time into smaller segments, but this system has achieved good results using a linear swath ground track sampled at start and end time.

Calculating the position of a satellite requires knowledge of its orbital parameters. The orbital parameters that define a satellite's orbit are traditionally recorded as a series of numbers in text called a Two-Line Element (TLE). Most satellites, excluding the International Space Station, have a relatively consistent orbit but are still perturbed by the gravity of the planets and thruster maneuvers to avoid debris. The United States Air Force is tasked with monitoring the current position and orbit of all detectable objects in the

Earth's orbit. The updated orbital parameters of non-classified spacecraft are published sub-daily in a TLE database called Space Track.

The *spacetrack* python package is used to query this database at the target time of a processing scene. The *pyephem* library is used to calculate the geographic coordinates of satellite positions from TLE to calculate a swath ground track polyline.

5.1.2.2 Cross-Track Swath Buffering

The bearing of the swath ground track at each satellite position is calculated from the two-dimensional arctangent between adjacent satellite positions. To project the cross-track boundaries of the swath, the geographic coordinates of each satellite position are transformed into Lambert Azimuthal Equal Area projection centered at the satellite position. Buffer points extending from each satellite position are calculated by offsetting these center-projected points in both directions perpendicular to bearing by a constant swath radius of 1,165 meters. These buffer points, along with the start and end positions of the satellite, re-projected to geographic coordinates, define the boundary polygon of the swath.

5.1.2.3 Meridian Geometry Splitting with Polar Transformation

In the case that the boundary polygon intersects the anti-meridian, where positive longitudes wrap back around to negative longitudes, the swath polygon is bisected by the anti-meridian into a multi-polygon. This is accomplished by transforming the swath polygon into polar coordinates, clipping by an anti-meridian wedge, and transforming the bisected polygons back into geographic coordinates. This prevents polygons from falling off the edge of the map and mixing positive and negative longitudes (Figure 12).

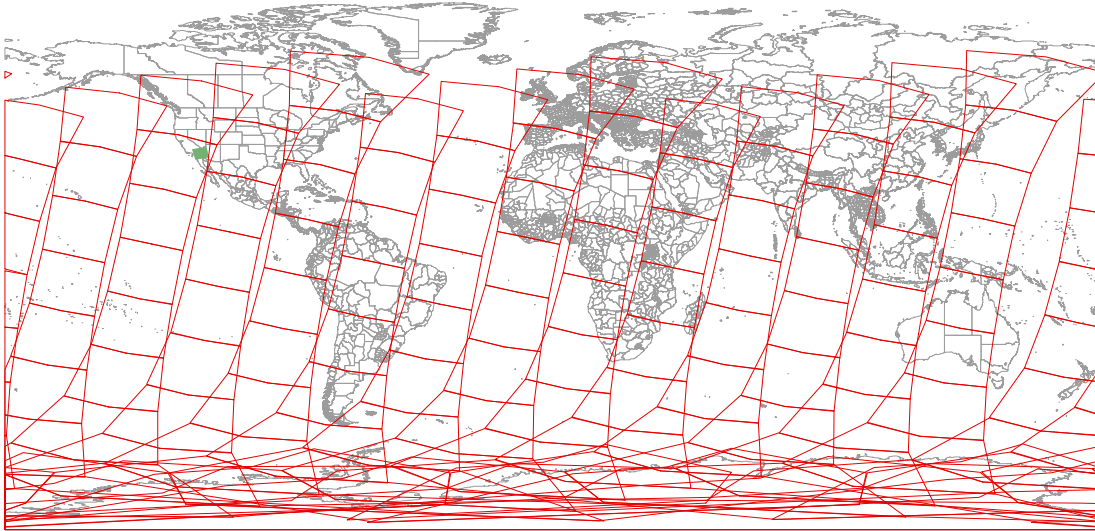


Figure 12. Example of daytime MODIS Terra swaths in one UTC day.

5.1.3 Polygon Intersection

The *shapely* library is used to handle geometric data. The underlying *GEOS* library is very efficient at testing polygon intersection for many potential matches. Out of potential source regions in a spatial and temporal search radius around the target regions, intersecting source regions are selected (Figure 13).

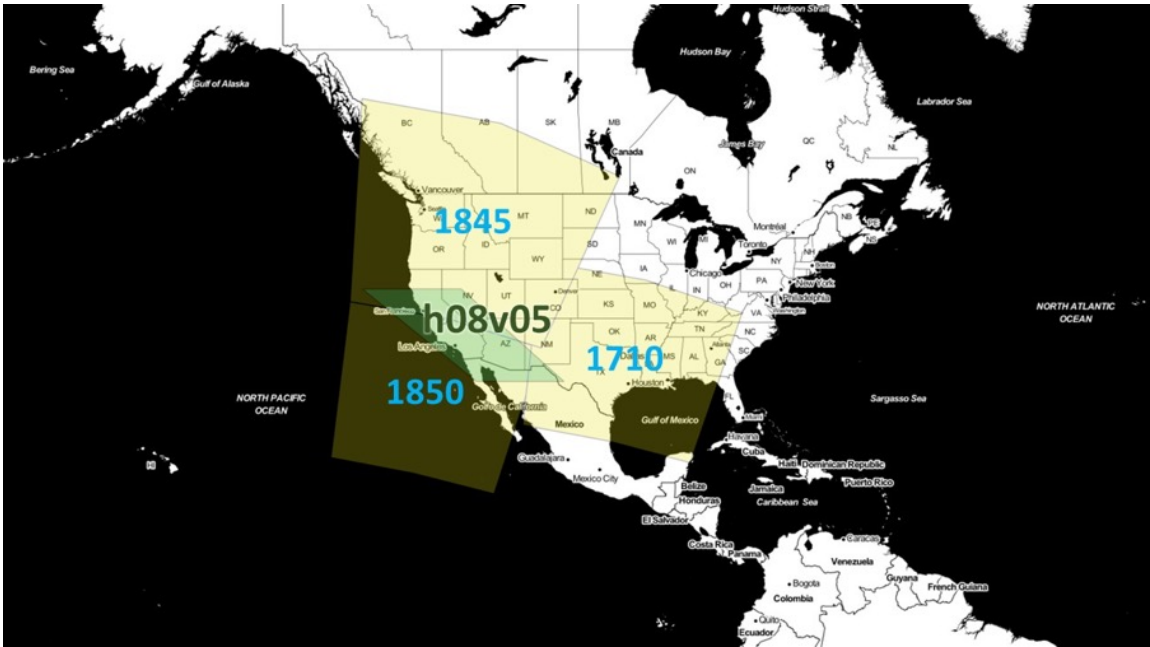


Figure 13. Example of MODIS swaths intersecting a MODIS land tile. In this example, the h08v05 tile intersects three Terra swaths: 1710, 1845, and 1850.

5.2 Address Resolution

Once the required scenes of source data have been identified through spatial and temporal intersection, these scene identifiers are resolved to remote addresses needed for file transfer. MODIS swath data are obtained from LAADS, MODIS tile data are obtained from LP-DAAC, reanalysis data are obtained from NCEP, and Landsat 8 data are obtained from Amazon Web Services.

5.2.1 LP-DAAC

The MODIS land products are obtained from the Land Processes Distributed Active Archive Center (LP-DAAC) in partnership with the United States Geological Survey (USGS). The MODIS land products are provided in sinusoidal projection, gridded using the MODIS land tile system. Tiles on this grid that fall outside of the sinusoidal projection of the Earth or contain only ocean are excluded from this acquisition. Addresses for source

data scenes hosted on the LP-DAAC are obtained using requests to the LP-DAAC Inventory API.

5.2.2 LAADS

The MODIS atmospheric products are obtained as swath datasets in HDF-EOS 2 format from the Level 1 and Atmosphere Archive and Distribution System (LAADS), hosted at Goddard Space Flight Center. Addresses for source data scenes hosted on LAADS are obtained using File Transfer Protocol (FTP).

5.2.3 NCEP

Reanalysis is a data assimilation scheme that combines the highest confidence data from many sources into low spatial resolution, high temporal resolution rasters. National Centers for Environmental Prediction (NCEP) reanalysis products are acquired as a secondary, gap-filling source of meteorological data. The reanalysis products are obtained from the National Oceanic and Atmospheric Administration (NOAA) Earth System Research Laboratory (ESRL) Physical Sciences Division (PSD). Addresses for source data scenes on NOAA's server are obtained using File Transfer Protocol (FTP).

5.2.4 Amazon Web Services

A joint effort between the USGS and NASA has made Landsat 8 data publicly available through the Amazon Web Services (AWS) cloud (Amazon Web Services, 2017). Individual bands from the Operational Land Imager (OLI) and Thermal Infrared Sensor (TIRS) are available in GeoTIFF format. Addresses for Landsat 8 bands are obtained using requests to the Development Seed API.

5.3 Data Transfer

Once all required scenes of source data have been identified and resolved to remote addresses, these data are transferred by feeding these addresses into *wget*. This is part of the standard set of GNU command line tools that are provided with Linux and OSX operating systems and can be installed on Windows. This mass-downloading tool handles completion of incomplete downloads and efficiently skips over previously completed downloads.

A demonstration for retrieving MODIS land tile scenes from the LP-DAAC and the NCEP FTP server using *wget* was provided by Augustin Muniz in the NASA DEVELOP New Mexico Water Resources I project of Summer 2015. This was expanded by Gregory Halverson in the NASA DEVELOP New Mexico Water Resources II project of Fall 2015 into the dynamic system described here with support for LAADS and extensibility for Landsat, ECOSTRESS, and future sources of data.

6 Processing

Once source data has been acquired, processing each target region runs in three stages. First, environmental variables from source datasets are ingested to a consistent format. Required variables are extracted from each scene and preprocessed in their original extent and resolution. These data are then mosaicked and projected onto the extent and resolution of each target scene. Once all inputs for the models have been produced as a set of equidimensional matrices, the sequence of models are run.

6.1 Data Ingest

Variable	Description	Product	Resolution	Projection
SZA	Solar Zenith Angle	MOD07	5 km	Swath
LC	Land-Cover Type	MCD12	500 m	Sinusoidal
KG	Climate Classification	Köppen-Geiger	30'	Geographic
AOT	Aerosol Optical Thickness	MOD04	5 km	Swath
COT	Cloud Optical Thickness	MOD06	5 km	Swath
Z_{top}	Cloud Top Height	MOD06	5 km	Swath
CF	Cloud Fraction	MOD06	5 km	Swath
α	Albedo	MCD43	1 km	Sinusoidal
	Albedo Fill	LTM	5 km	Sinusoidal
$P_{surface}$	Surface Pressure	MOD07	5 km	Swath
T_a	Air Temperature	MOD07	5 km	Swath
	Air Temperature Fill	air.sig995	2°30'	Geographic
T_d	Dew-Point Temperature	MOD07	5 km	Swath
	Dew-Point Temperature Fill	rhum.sig995	2°30'	Geographic
T_{opt}	Optimum Temperature	LTM	5 km	Sinusoidal
LST	Land-Surface Temperature	MOD11	1 km	Sinusoidal
ϵ	Emissivity	MOD11	1 km	Sinusoidal
NDVI	Vegetation Index	MOD13	500 m	Sinusoidal
$f_{APARmax}$	Photosynthetically Active Radiation	LTM	5 km	Sinusoidal
GPP	Gross Primary Production	MOD17	1 km	Sinusoidal

Table 1. Summary of retrieved forcing datasets.

Sources of data for the pipeline include complex datasets with many variables, stored in a variety of formats, resolutions, and projections (Table 1). These variables are often

compressed by scaling floating point values to short integers with a convention called Digital Numbers (DNs). Digital Numbers typically have a linear relationship with the variables they represent, and are reconstituted into actual units of observation with multiplicative and additive components that are attached as metadata. There is no universal convention for representing cells of no data as integers, so a fill value such as -999 is usually included in metadata as well. Each variable of forcing data is loaded from the local copy of its source dataset, scaled to real units, filtered by associated quality flags, and written to temporary storage using HDF5. The methods and implementation of ingest for each variable described here were developed and tested with the extensive collaboration of Dr. Laura Jewell of the ECOSTRESS mission.

Landsat 8	Band	Wavelength (μm)	Resolution (m)
OLI	L8B1 - Ultra Blue (coastal/aerosol)	0.43 - 0.45	30
	L8B2 - Blue	0.45 - 0.51	30
	L8B3 - Green	0.53 - 0.59	30
	L8B4 - Red	0.64 - 0.67	30
	L8B5 - Near Infrared (NIR)	0.85 - 0.88	30
	L8B6 - Shortwave Infrared (SWIR) 1	1.57 - 1.65	30
	L8B7 - Shortwave Infrared (SWIR) 2	2.11 - 2.29	30
	L8B8 - Panchromatic	0.50 - 0.68	15
	L8B9 - Cirrus	1.36 - 1.38	30
TIRS	L8B10 - Thermal Infrared (TIRS) 1	10.60 - 11.19	100
	L8B11 - Thermal Infrared (TIRS) 2	11.50 - 12.51	100

Table 2. Landsat 8 Operational Land Imager (OLI) and Thermal Infrared Sensor (TIRS) bands (USGS, 2016).

The Landsat evapotranspiration product uses Landsat 8 top-of-atmosphere reflectance for LST (6.1.13), albedo (6.1.8), and NDVI (6.1.15).

The Landsat 8 satellite includes nine 15 to 30-meter resolution shortwave bands on the Operational Land Imager (OLI) and two 100-meter resolution longwave bands on the Thermal Infrared Sensor (TIRS) (Table 2) (USGS, 2016).

6.1.1 Solar Zenith Angle

Solar zenith angle is the angle of the sun from zenith, the highest point in its path through the sky. This angle is calculated astronomically. The day angle (Γ radians) is calculated as a function of the day of year (d_n days) (Equation 1) (Saleem, 2016).

$$\Gamma = \frac{2\pi * (d_n - 1)}{365}$$

Equation 1. Formula to calculate day angle from day of year.

Solar declination (δ radians) is calculated as a function of day angle (Γ radians) (Equation 2) (Saleem, 2016).

$$\delta = [0.006918 - 0.39912 * \cos(\Gamma) + 0.070257 * \sin(\Gamma) - 0.006758 * \cos(2\Gamma) + 0.000907 * \sin(2\Gamma) - 0.002697 * \cos(3\Gamma) + 0.00148 * \sin(3\Gamma)]$$

Equation 2. Formula to calculate solar declination from day angle.

Sunrise hour angle (SHA degrees) is calculated using the sunrise equation as a function of solar declination (δ degrees) and latitude (ϕ radians) (Equation 3).

$$SHA = \cos^{-1}(-\tan(\phi) * \tan(\delta)) * \frac{180}{\pi}$$

Equation 3. Sunrise equation for hour angle from latitude and solar declination.

The hour of sunrise (SH hours) (Equation 4) and the number of daylight hours (DL hours) are calculated from the sunrise hour angle (SHA degrees) (Equation 5). These are used in the calculation of diurnal air temperature and daily integration of net radiation.

$$H_{sunrise} = 12 - \frac{SHA}{15}$$

Equation 4. Sunrise hour from sunrise hour angle.

$$DL = \frac{2}{15} * SHA$$

Equation 5. Daylight hours from sunrise hour angle.

The hour angle (HA radians) for the target time is a function of the hour of day (H hours) (Equation 6).

$$HA = (H * 15 - 180) * \frac{\pi}{180}$$

Equation 6. Equation for hour angle from hour of day.

Solar zenith angle (SZA degrees) is calculated from solar declination, hour angle, and latitude (Equation 7).

$$SZA = \cos^{-1}(\sin(\phi) * \sin(\delta) + \cos(\phi) * \cos(\delta) * \cos(HA)) * \frac{180}{\pi}$$

Equation 7. Equation for solar zenith angle from solar declination, hour angle, and latitude.

6.1.2 IGBP Land Cover Classification

The International Geosphere-Biosphere Programme (IGBP) created a standard set of land type classifications that can be produced from remote sensing data. There are IGBP land type products from the MODIS, CERES, and VIIRS sensors. The MODIS data product, MCD12 (Strahler, et al., 1999), is produced annually, and is available until 2013. The pipeline reads IGBP classification from the target year's MCD12 product and reverts to the 2013 product for succeeding years. Future work on the pipeline includes upgrading IGBP ingest from MODIS to VIIRS to keep up-to-date records of land type classification. These classifications are used together with the Köppen-Geiger climate classifications (Figure 14) for gap-filling of albedo data (6.1.8).

6.1.3 Köppen-Geiger Climate Classification

The Köppen-Geiger Climate Classification categorized the Earth's surface into climate zones (Figure 14) (Institute for Veterinary Public Health, 2017). This is used to calculate climatic trends in albedo gap-filling (6.1.8). A static lookup table of climate classifications is loaded and sampled to the target scene.

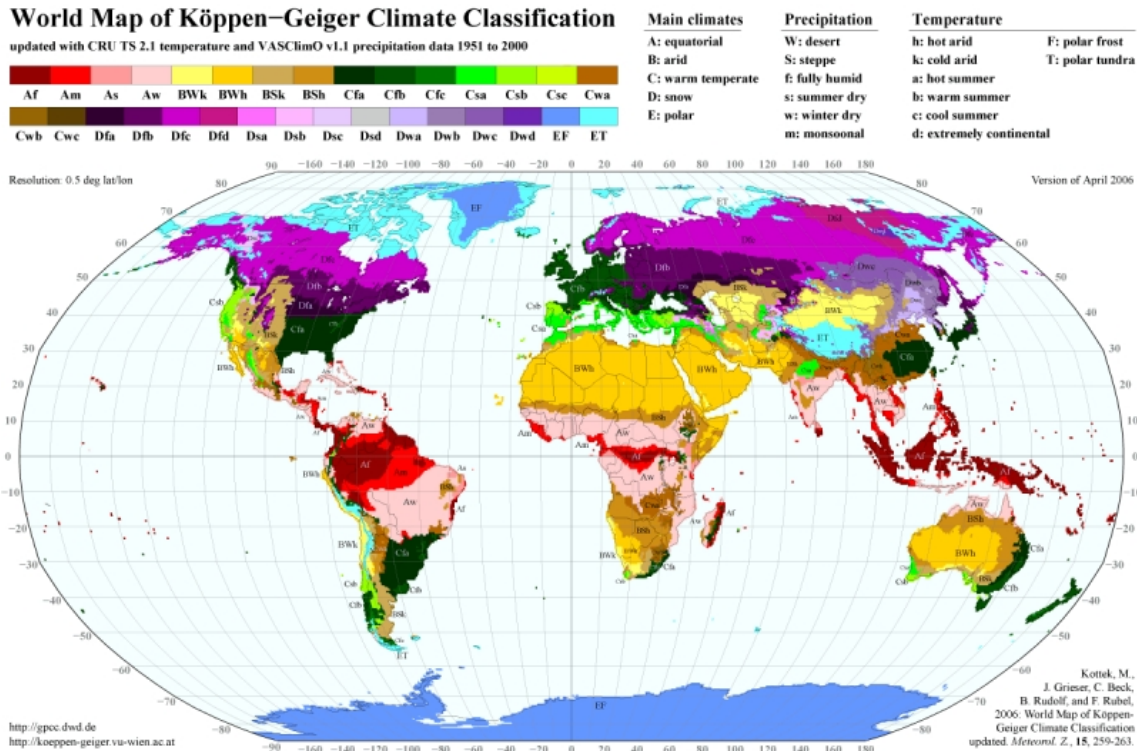


Figure 14. Köppen-Geiger climate classification (Institute for Veterinary Public Health, 2017).

6.1.4 Aerosol Optical Thickness

Aerosol optical thickness (AOT) is a measure of how much dust in the air blocks out the light of the sun. This variable is extracted from the MOD04 aerosol product (Levy, Remer, Tanre, Mattoo, & Kaufman, 2009). Aerosol optical thickness at 550 nm is used as a variable of atmospheric transmissivity in estimating the radiative transfer of the sun’s energy through the atmosphere to the surface.

6.1.5 Cloud Optical Thickness

As a measure of atmospheric transmissivity, like AOT (6.1.4), cloud optical thickness (COT) represents how much the light of the sun is blocked out by water vapor. This variable is loaded from the MOD06 cloud product (Menzel, Frey, & Baum, 2010) and used as a parameter for the radiative transfer of incoming shortwave radiation (6.3.2.1).

6.1.6 Cloud Top Height

The altitude of the top of the clouds (Z_{top} m) is computed from the MOD06 (Menzel, Frey, & Baum, 2010) cloud top pressure (P_{top} hPa), surface pressure ($P_{surface}$ hPa), and surface temperature ($T_{surface}$ K) (Equation 8). This conversion of pressure to altitude uses a gas constant for dry air (R) (American Meteorological Society, 2014) and acceleration of gravity (g) (Table 3).

Name	Description	Value
R	Gas Constant of Dry Air	287.053 J K ⁻¹ kg ⁻¹
g	Acceleration of Gravity	9.8 m s ⁻²

Table 3. Constants used in hypsometric equation.

$$Z_{top} = \left(\log(P_{surface}) - \log(P_{top}) \right) * R * \frac{T_{surface}}{g}$$

Equation 8. Hypsometric equation for cloud top height from cloud top pressure, surface pressure, and surface temperature.

6.1.7 Cloud Fraction

The fraction of the sky covered by clouds for any given raster cell is loaded from the MOD06 cloud product (Menzel, Frey, & Baum, 2010). This variable is used in calculating the bi-directional reflectance function of albedo (6.1.8).

6.1.8 Albedo

Albedo is a core variable in calculating the surface energy balance of the planet. It represents the fraction of incoming shortwave radiation that is reflected as outgoing shortwave radiation (6.3.2.2). The main source of albedo data for the MODIS PT-JPL product is the MCD43 BRDF product (Strahler, et al., 1999).

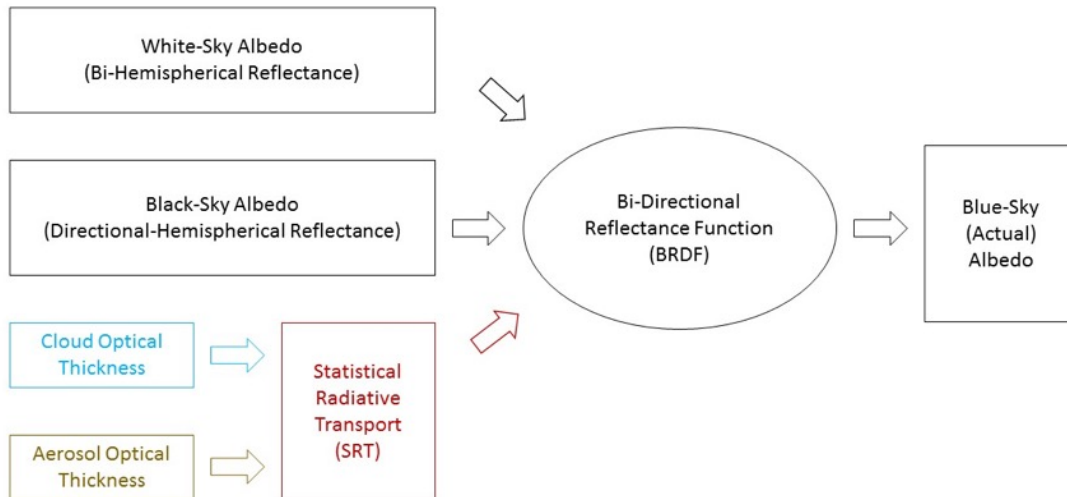


Figure 15. Flowchart of the calculation of albedo from BRDF parameters.

The bi-directional reflectance function (BRDF) separates albedo into directional-hemispheric reflectance, also called black-sky albedo, and bi-hemispherical reflectance, also called white-sky albedo. This separation takes diffuse and direct illumination with backscattering into account. The actual reflectance of shortwave radiation, also called blue-sky albedo, is calculated from these BRDF parameters with values of statistical radiative transport queried from a lookup table by cloud optical thickness and aerosol optical thickness (Figure 16).

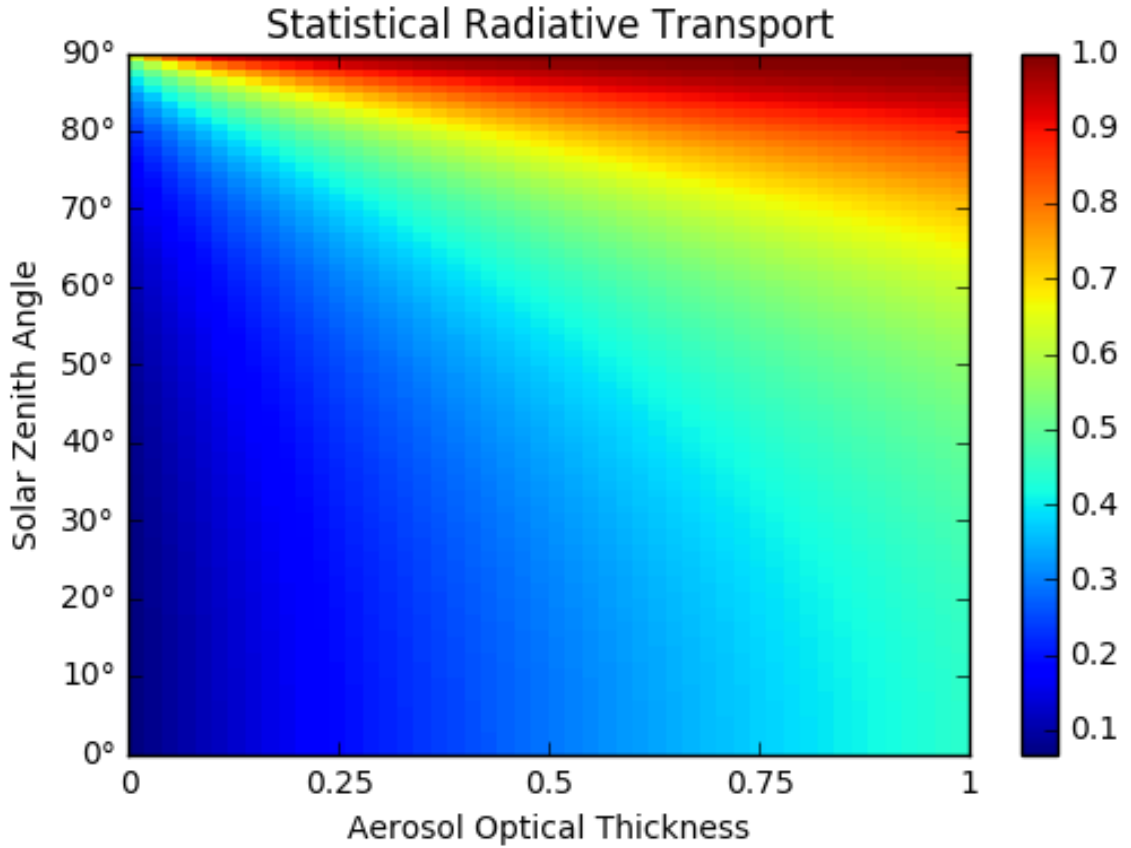


Figure 16. Lookup table of statistical radiative transport from aerosol optical thickness and solar zenith angle.

When the fraction of the sky covered by clouds (6.1.7) is greater than 70%, blue-sky albedo is assumed to be white-sky albedo. For clear sky conditions, statistical radiative transport (SRT) is factored into white-sky (α_{white}) and black-sky (α_{black}) albedo to derive blue-sky albedo (α_{blue}) (Equation 9).

$$\alpha_{blue} = \alpha_{white} * SRT + \alpha_{black} * (1 - SRT)$$

Equation 9. Formula for blue-sky albedo from white-sky and black-sky albedos.

Albedo is gap-filled using long-term climatic means. The MODIS shortwave BRDF parameters were averaged for a decade. These decadal averages are loaded, averaged by IGBP, Köppen-Geiger classification (Figure 14), and applied to matching land and climate classifications in areas of missing data in the albedo raster.

For the ECOSTRESS and Landsat evapotranspiration products, shortwave albedo will be calculated here from Landsat 8 bands. No methodology could be found using Landsat to replace the blue sky and black sky albedo from MODIS (6.1.8). Instead, shortwave albedo will be estimated using a linear relationship with the Landsat 8 shortwave bands (Yale University, 2017):

$$\alpha = 0.356 * B2 + 0.130 * B3 + 0.373 * B4 + 0.085 * B5 + 0.072 * B6 - 0.018$$

Equation 10. Albedo from Landsat 8 bands (Yale University, 2017).

The Yale equation for Landsat albedo (Yale University, 2017) is fitted for the previous generations of Landsat, so this assumes an identical spectral response in the Landsat 8 bands, which are generally within a few nanometers of the wavelength ranges of the original Landsat bands.

6.1.9 Surface Pressure

Atmospheric or barometric air pressure is the pressure exerted by the weight of air in the atmosphere. This pressure is highest at lower elevations near sea-level and decreases at high altitudes, so pressure is often used to indicate the altitude of an atmospheric measurement. The pressure of the air in the near-surface atmosphere is loaded from the MOD07 atmospheric profiles product (Seemann, Borbas, Li, Menzel, & Gumley, 2006) and used to vertically interpolate air temperature and dew point temperature to the near-surface level (Equation 11).

6.1.10 Air Temperature

Air temperature near the surface, at about two meters' altitude, is used to determine the water capacity of the air (2.2). The MOD07 atmospheric profiles product (Seemann, Borbas, Li, Menzel, & Gumley, 2006) provides soundings of air temperature at altitudinal

profiles corresponding to atmospheric pressure levels. These atmospheric profiles are vertically interpolated to the two-meter reference height using surface pressure.

The cells of this raster represent atmospheric columns of temperature at pressure profiles with altitude increasing as pressure decreases. In each atmospheric column, the temperature given at the nearest lower (T_{lower}) and higher (T_{upper}) altitudes and their corresponding pressures (P_{lower} and P_{upper}) are selected for interpolation. This interpolation uses the hypsometric constants to convert pressure to altitude (Table 3). Surface temperature ($T_{surface}$) is interpolated to surface pressure ($P_{surface}$) (Equation 11).

$$T_{surface} = T_{lower} + (T_{lower} - T_{upper}) * \frac{\frac{R}{g} * (T_{upper} + 273.16) * \log\left(\frac{P_{lower}}{P_{upper}}\right)}{\frac{R}{g} * (T_{lower} + 273.16) * \log\left(\frac{P_{surface}}{P_{lower}}\right)}$$

Equation 11. Vertical interpolation of atmospheric temperature profiles.

Gap-filling data for this variable is obtained from the NCEP air.sig995 product, which comes already interpolated to the near-surface sigma 0.995 level (NOAA Earth System Research Laboratory, 2017).

6.1.11 Dew-Point Temperature

The dew point is the temperature at which the air is saturated with water vapor (2.2), so it is a measure of humidity as a temperature. Ingest of dew-point temperature follows a similar methodology to air temperature. Atmospheric profiles of dew-point temperature soundings from MODIS are loaded from the MOD07 atmospheric profiles product (Seemann, Borbas, Li, Menzel, & Gumley, 2006) and vertically interpolated to the near-surface level using surface pressure (Equation 11).

Dew-point temperature is gap-filled using NCEP reanalysis. Relative humidity (RH) is loaded from the rhum.sig995 product, and converted to dew-point temperature (T_d K) using air temperature (T_a K) (Equation 12) (Lawrence, 2005).

$$T_d = T_a - \frac{(100 - RH)}{5}$$

Equation 12. Formula for dew-point temperature from air temperature and relative humidity.

6.1.12 Optimum Temperature

Optimum temperature is the air temperature of optimum phenology, when plants are most active. Phenology was calculated from a decade of net radiation (R_n W m⁻²) (Equation 25), air temperature (T_a C), SAVI (Equation 27), and vapor pressure deficit (VPD kPa) data (Equation 13). Optimum temperature was selected from air temperature at the annual maximum of phenology.

$$phen = \frac{R_n * T_a * SAVI}{VPD}$$

Equation 13. Formula for phenology from net radiation, air temperature, SAVI, and vapor pressure deficit.

Optimum temperature in Celsius is read from a lookup table of the decadal mean of these annual maxima. This variable is used to determine plant temperature constraint (Equation 39).

6.1.13 Land-Surface Temperature

For the MODIS PT-JPL product, the MOD11A1 product (Wan, 1999) provides 1 km resolution sinusoidal tiles of daytime land-surface temperature (LST) in Kelvin. LST is used to estimate the rate of outgoing longwave radiation (Equation 24).

For the Landsat PT-JPL product, the brightness temperatures of Landsat 8 bands 10 (BT_{10}) and 11 (BT_{11}) are loaded using the USGS method for conversion of DN's to at-satellite

brightness temperature (USGS, 2016). The brightness temperatures of both thermal bands are combined into LST using the Split-Window Algorithm (Jiménez-Muñoz, Sobrino, Skokovic, Mattar, & Cristóbal, 2014) with a constant water vapor content (w) of 1.2 grams per square centimeter (Equation 15). This method was adapted from the CRAN-R water package implementation of METRIC (Olmedo, Ortega-Farias, Fonseca-Luengo, de la Fuente-Saiz, & Peñailillo, 2017).

$$\Delta BT = BT_{10} - BT_{11}$$

Equation 14. Difference in brightness temperature between Landsat 8 band 10 and 11.

$$LST = BT_{10} + 1.378 * \Delta BT + 0.183 * \Delta BT^2 - 0.268 + (54.3 - 2.238 * w) * (1 - \varepsilon)$$

Equation 15. Split-window algorithm for LST from Landsat 8 (Jiménez-Muñoz, Sobrino, Skokovic, Mattar, & Cristóbal, 2014).

In the collaboration with the ECOSTRESS mission (1.2), the ECOSTRESS level 3 product will read the ECOSTRESS level 2 diurnal LST product here instead of MODIS.

6.1.14 Emissivity

Emissivity is the ratio of energy that an object emits to the amount of energy it would emit if it were a black body or perfect emitter of energy. Emissivity is used to scale the Stefan Boltzmann relationship between temperature and energy transfer (Equation 24). This variable is usually always included with estimates of LST. Both LST and emissivity are ingested from the MOD11 product (Wan, 1999).

The Landsat product calculates emissivity using a method adapted from the CRAN-R water package implementation of METRIC (Olmedo, Ortega-Farias, Fonseca-Luengo, de la Fuente-Saiz, & Peñailillo, 2017). Leaf Area Index (LAI) is calculated from NDVI (Equation 16), and emissivity is calculated from LAI (Equation 17).

$$LAI = 0.5724 + 0.0989 * NDVI - 0.0114 * NDVI^2 + 0.0004 * NDVI^3$$

Equation 16. Leaf Area Index from Normalized Difference Vegetation Index.

$$\varepsilon = 0.97 + 0.0033 * LAI$$

Equation 17. Surface emissivity from Leaf Area Index.

6.1.15 Normalized Difference Vegetation Index

The spectral response of chlorophyll-alpha is very high in the near infrared and relatively low in red light. Normalizing the reflectance of near-infrared radiation to red light generates an index of how much vegetation is on the ground. This index is called the normalized difference vegetation index (NDVI). The MOD13A1 product (Huete, Justice, & Leeuwen, 1999) provides a 16-day composite of NDVI in sinusoidal tile format at 500 m resolution. This variable is used to constrain estimates of transpiration released by plants. For the ECOSTRESS and Landsat evapotranspiration products, NDVI is calculated from the standard normalized difference of Landsat 8 near-infrared band 5 (B5) and red band 4 (B4):

$$NDVI = \frac{B5 - B4}{B5 + B4}$$

Equation 18. NDVI from Landsat 8 bands.

6.1.16 Maximum Fraction of Absorbed Photosynthetically Active Radiation

The maximum fraction of absorbed photosynthetically active radiation is the annual maximum at which plants absorb energy. This value was calculated as a lookup table by calculating f_{APAR} (Equation 28) for a decade of MODIS NDVI (6.1.15), and taking the mean of the annual maxima. Like optimum temperature (6.1.12), this mean is read as a look up table.

6.1.17 Gross Primary Production

Gross primary production is a measure of the growth of vegetation through photosynthesis. The MOD17 product provides GPP in kilograms of carbon at 1 km spatial resolution over an 8-day period, half the orbit of MODIS. This 8-day GPP is divided by 8 to estimate daily intake of carbon and then scaled from kilograms to grams for use in calculating Water Use Efficiency.

6.2 Projection

Ingested data that are preprocessed in their original geolocation must be mosaicked and resampled into consistent tiles for model processing. The MODIS PT-JPL product is designed to run on the Sinusoidal Tile Grid (5.1.1.1) at either 5 km or 1 km resolution. The 5 km resolution tiles use 240 by 240 matrices with a cell size of 4,633.13 meters, and the 1 km resolution uses 1200 by 1200 matrices with a cell size of 926.63 meters. The Landsat PT-JPL product follows the Landsat convention of using locally centered Universal Transverse Mercator (UTM) projections with a cell size of 30 meters. ECOSTRESS, aerial data, and other potential products that process as swaths use a pair of geolocation arrays as their destination.

Support for processing both swath and grid spatial extents as the source or destination requires support for four combinations: projecting from grid to grid, projecting from swath to grid, resampling from grid to swath, or resampling from swath to swath (Figure 17).

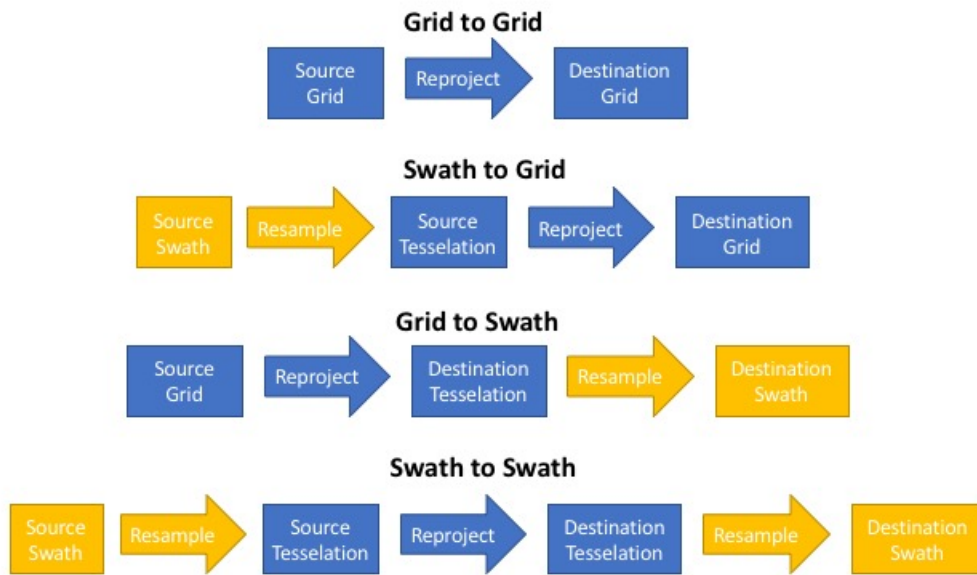


Figure 17. Four paths of projection.

6.2.1 Grid to Grid

The easiest case for projection occurs when both the source and destination are grids of coordinates sampled at equal intervals in two dimensions. The *rasterio* package is used to re-project between grids in python.

6.2.2 Swath to Grid

A swath cannot be directly re-projected because it's not already projected. Resampling techniques such as K-D Tree or Delaunay Triangulation do not produce good results when there is a major disparity in spatial scale between source and destination, but re-projection does. Swaths must be first projected to allow re-projection to the destination grid. To accomplish this, the source swath is resampled to a grid representative of the extent and spatial resolution of the swath. This now gridded source data is then re-projected to the destination using the grid-to-grid (6.2.1) process.

6.2.3 Grid to Swath

In the case that gridded data must be made to match the coordinates of a swath, a representative grid is generated for destination similar to the swath-to-grid method (6.2.2). The grid-to-grid (6.2.1) process re-projects the data to the temporary destination grid, then the destination grid is resampled to the swath coordinates.

6.2.4 Swath to Swath

The most difficult case is when both the source and destination are swaths that are not georeferenced. Resampling directly between geolocation arrays does not always produce good results. In this case, temporary grids must be used to represent both the source and destination.

6.3 Model Processing

The Sinusoidal Tile Grid (Figure 10) used by MODIS land products is used as the basic spatial unit of processing to generate the MODIS PT-JPL product at 5 km or 1 km. Once all source data have been preprocessed into real variables and projected into this format, a series of environmental modeling formulas are run on these data to generate the product. These models have been divided into three stages reflecting their origins in literature, FLiES to calculate incoming shortwave radiation, BESS to calculate net radiation, and PT-JPL to calculate latent heat flux.

6.3.1 Forest Light Environmental Simulator

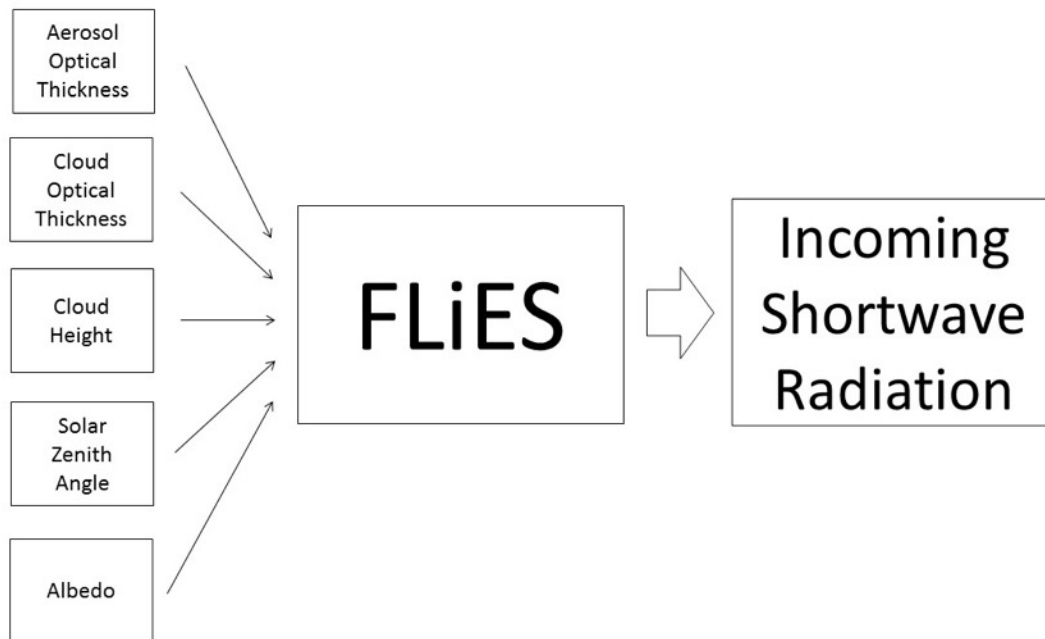


Figure 18. Flowchart of the Forest Light Environmental Simulator.

6.3.1.1 Radiative Transfer Lookup Table

Radiative transfer equations consume a great deal of processing power. A routine strategy to work with radiative transfer algorithms is to compile a lookup table of pre-computed values. Following the example of Dr. Hideki Kobayashi and Dr. Youngryel Ryu (3.2.4), incoming shortwave radiation is queried from a lookup table indexed by discrete quantization of solar zenith angle, cloud type, cloud top height (Equation 8), cloud optical thickness (6.1.5), aerosol optical thickness (6.1.4), land surface albedo (6.1.8), and climate type (6.1.3)(Figure 18)(Table 4).

Variable	Factors
Solar Zenith Angle	5, 10, 15, 20, 25, 30, 35, 40, 45, 50, 55, 60, 65, 70, 75, 80, 85
Cloud Type	Cloud-Free, Stratus Continental, Cumulous Continental
Cloud Top Height (meters)	1000, 3000, 5000, 7000, 9000
Cloud Optical Thickness	0.1, 0.5, 1, 5, 10, 20, 40, 60, 80, 110
Aerosol Optical Thickness	0.1, 0.3, 0.5, 0.7, 0.9
Land Surface Albedo	0.1, 0.4, 0.7
Climate Type	Tropical, Temperate, Snow

Table 4. Quantization factors of FLiES lookup table indices (Ryu, et al., 2011).

6.3.1.2 De-Quantization Interpolation

Quantization of solar zenith angle into 5 degree bands as an index to the FLiES lookup table produces a severe banding pattern in incoming shortwave that persists as a visible artifact in derived net radiation and latent heat flux images (Figure 19) (Ryu, et al., 2011). To compensate for this, the table is queried at the two closest indices of solar zenith angle and interpolated with respect to the input value to produce a smooth raster of incoming shortwave radiation (Figure 19).

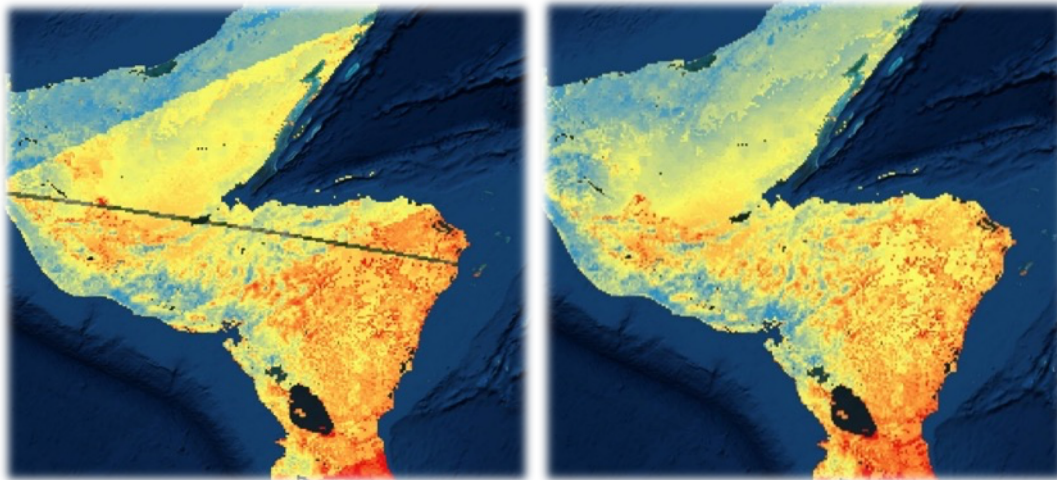


Figure 19. Net radiation without using interpolation in FLiES query (left) and net radiation using interpolation in FLiES query (right).

6.3.2 Breathing Earth Systems Simulator

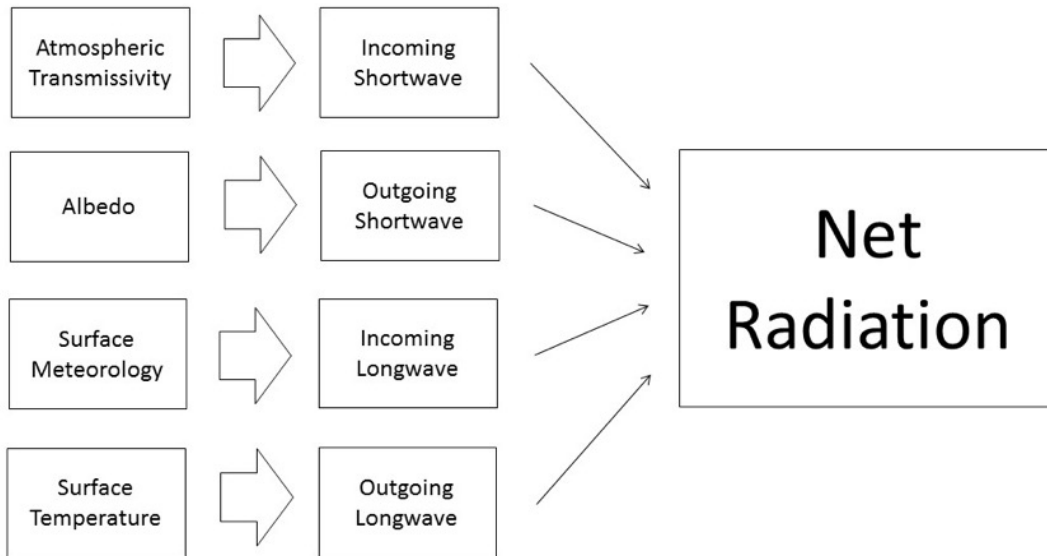


Figure 20. Flowchart of the Breathing Earth Systems Simulator.

Inspired by Dr. Youngryel Ryu’s system (3.2.4), and following the example set forth by Dr. Greg Moore and Dr. Manish Verma (Verma, et al., 2016), this adaptation of BESS uses atmospheric transmissivity to calculate incoming shortwave radiation with the FLiES model (6.3.1), albedo for outgoing shortwave, surface meteorology for incoming longwave, and surface temperature for outgoing longwave (Figure 20).

6.3.2.1 Incoming Shortwave Radiation

Incoming shortwave radiation is loaded from FLiES (6.3.1) output as the core driver of energy available at the Earth’s surface.

6.3.2.2 Outgoing Shortwave Radiation

Outgoing shortwave radiation (SW_{out}) is calculated as the product of incoming shortwave radiation (SW_{in}) and blue-sky shortwave albedo (α_{blue}) (Equation 19). This represents the amount of the sun’s energy that reaches the Earth’s surface but is immediately reflected up through the atmosphere into space.

$$SW_{out} = SW_{in} * \alpha_{blue}$$

Equation 19. Formula for outgoing shortwave radiation.

6.3.2.3 Incoming Longwave Radiation

Not all of the energy reflected into space makes it back out of the atmosphere. Green-house gases like carbon dioxide, methane, and water vapor absorb energy passing through the atmosphere and then emit some of it back down to the surface. This atmospheric blanket of gases keeps the Earth warm in a delicate balance. The energy of the green-house effect that reaches the surface is incoming longwave radiation.

Clear-sky conditions are assumed for values of cloud optical thickness that are very low (< 0.1) or absent. Clear-sky incoming longwave radiation (LW_{in} $W m^{-2}$) is calculated using a Stefan Boltzmann constant (σ) of 5.67 with air temperature (T_a K) (Equation 22), scaled by atmospheric emissivity (ϵ_{clear}) determined by air temperature (T_a K) and water vapor pressure (E_a Pa) (Equation 21) (Verma, et al., 2016). Water vapor pressure (E_a Pa) is calculated from dew-point temperature (T_d K) (Equation 20).

$$E_a = 2.1718 * 10^{10} * e^{\left(\frac{-4157}{T_d - 33.91}\right)}$$

Equation 20. Actual water vapor pressure from dew-point temperature.

$$\epsilon_{clear} = 1 - \left(1 + \frac{0.465 * E_a}{T_a}\right) * e^{-\left(1.2 + 3 * \frac{0.465 * E_a}{T_a}\right)^{0.5}}$$

Equation 21. Formula for clear-sky atmospheric emissivity.

$$LW_{in} = \epsilon_{clear} * \sigma * T_a^4$$

Equation 22. Formula for incoming longwave radiation in clear-sky conditions.

Under cloudy conditions, the atmosphere is assumed to emit energy as a black body, and incoming longwave (LW_{in} W m⁻²) is calculated without taking emissivity into account (Equation 23) (Verma, et al., 2016).

$$LW_{in} = \sigma * T_a^4$$

Equation 23. Formula for incoming longwave radiation in cloudy conditions.

6.3.2.4 Outgoing Longwave Radiation

Outgoing longwave radiation (LW_{out} W m⁻²) is the rate at which the surface emits energy. Outgoing longwave radiation is calculated from land-surface temperature (LST K) and emissivity (ϵ) using a Stefan Boltzmann constant (σ) of 5.67 (Equation 24) (Verma, et al., 2016).

$$LW_{out} = \epsilon * \sigma * LST^4$$

Equation 24. Stefan Boltzmann equation for outgoing longwave radiation from land-surface temperature and emissivity.

6.3.2.5 Net Radiation

Net radiation (R_n W m⁻²) is calculated from the balance of incoming shortwave radiation (SW_{in} W m⁻²), outgoing shortwave radiation (SW_{out} W m⁻²), incoming longwave radiation (LW_{in} W m⁻²), and outgoing longwave radiation (LW_{out} W m⁻²) (Equation 25) (Verma, et al., 2016). This represents the amount of energy left over at the surface, controlling for major ingresses and egresses of shortwave and longwave radiation.

$$R_n = (SW_{in} - SW_{out}) + (LW_{in} - LW_{out})$$

Equation 25. Formula for net radiation given surface energy balance components.

6.3.2.6 Daily Integration of Net Radiation

The daily average of net radiation (R_{nd} W m⁻²) is calculated from instantaneous net radiation (R_n W m⁻²) using a sinusoidal integration across daylight hours (Equation 26) (Verma, et al., 2016).

$$R_{nd} = \frac{1.6 * R_n}{\pi * \sin\left(\pi * \frac{H - H_{sunrise}}{H_{sunset} - H_{sunrise}}\right)}$$

Equation 26. Sinusoidal integration of instantaneous net radiation across daylight hours for daily average.

6.3.3 Priestley-Taylor Jet Propulsion Laboratory

Following Dr. Joshua Fisher's example (Fisher, Tu, & Baldocchi, 2008) with minor improvements under his direction, the PT-JPL model (3.2.5) is implemented here. Forcing data required for PT-JPL includes air temperature, humidity, net radiation, vegetation index, and photosynthetically absorbed radiation (Table 5). Air temperature is ingested both as an instantaneous value at the time of observation and as a mean at the monthly temporal scale. Humidity and vegetation are averaged to the monthly scale. Both instantaneous and daily net radiation are used.

Variable	Description	Temporal Scale	Section
T_a	Air Temperature	Instantaneous/Monthly	6.1.10
E_a	Water Vapor Pressure		6.3.2.3
R_n	Net Radiation	Instantaneous	6.3.2.5
R_{nd}	Daily Net Radiation	Daily	6.3.2.6
NDVI	Vegetation Index	Monthly	6.1.15
T_{opt}	Optimum Temperature	Annual	6.1.12
$f_{APARmax}$	Photosynthetically Absorbed Radiation		6.1.16

Table 5. Forcing variables for PT-JPL model.

6.3.3.1 PT-JPL Latent Heat Flux Partitioning

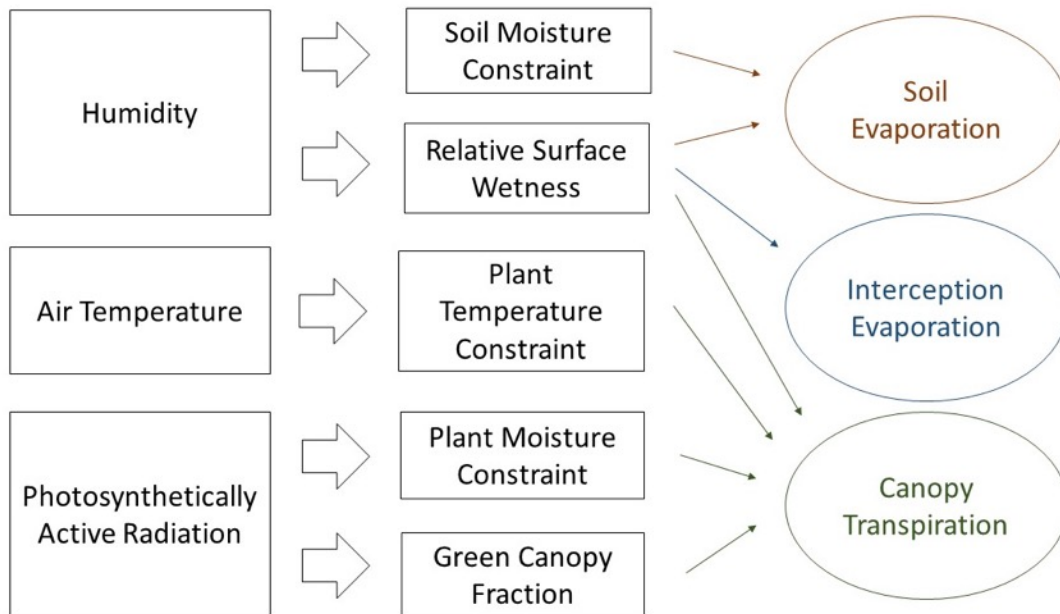


Figure 21. Flowchart of PT-JPL partitioning.

The Priestley-Taylor Jet Propulsion Laboratory (PT-JPL) model of evapotranspiration partitions latent heat flux into three components: canopy transpiration, interception evaporation, and soil evaporation (Figure 21). This is accomplished by estimating a series of biophysical constraints applied to the Priestley-Taylor equation: the soil moisture constraint, relative surface wetness, plant temperature constraint, plant moisture constraint, and green canopy fraction (Figure 21).

6.3.3.2 Vegetation

Soil-adjusted vegetation index (SAVI) is a correction of NDVI that takes red and near-infrared extinction through canopy cover into account. PT-JPL derives SAVI from a linear relationship with NDVI (Equation 27). NDVI is first clipped to a range of zero to one.

$$SAVI = NDVI * 0.45 + 0.132$$

Equation 27. Linear conversion of NDVI to SAVI.

The fraction of absorbed photosynthetically active radiation is calculated from a linear relationship with SAVI (Equation 28).

$$f_{APAR} = SAVI * 1.3632 - 0.048$$

Equation 28. Linear conversion of SAVI to fraction of absorbed photosynthetically active radiation.

The fraction of intercepted photosynthetically active radiation is a minor offset from NDVI (Equation 29).

$$f_{IPAR} = NDVI - 0.05$$

Equation 29. Fraction of intercepted photosynthetically active radiation from NDVI.

Leaf area index (LAI m² m⁻²) is the ratio of the area of leaves to the area of the ground. LAI is calculated from a logarithmic relationship with f_{IPAR} (Equation 30).

$$LAI = -2 * \log(1 - f_{IPAR})$$

Equation 30. Leaf area index from fraction of intercepted photosynthetically active radiation.

Soil heat flux (G W m⁻²) is calculated in watts per square meter as a fraction of net radiation (R_n W m⁻²) constrained by the fraction of intercepted photosynthetically active radiation (f_{IPAR}) (Equation 31) (Fisher, Tu, & Baldocchi, 2008), where f_{IPAR} is constrained between zero and one.

$$G = R_n * (0.05 + (1 - f_{IPAR}) * 0.265)$$

Equation 31. Formula for soil heat flux.

6.3.3.3 Meteorology

Saturation vapor pressure (E_{sat} kPa) is the maximum possible pressure of water vapor in the air at its current temperature. Saturation vapor pressure is calculated from an

exponential relationship with air temperature at the monthly temporal scale (T_{am} C) (Equation 32).

$$E_{sat} = 0.611 * e^{\left(\frac{17.27 * T_a}{T_a + 237.7}\right)}$$

Equation 32. Saturation vapor pressure from air temperature.

Vapor pressure deficit (VPD kPa) is the amount of water vapor pressure than can still be added to the air at its current temperature before it reaches saturation. VPD is calculated as the difference of saturation (E_{sat} kPa) and actual (E_a kPa) water vapor pressure (Equation 33).

$$VPD = E_{sat} - E_a$$

Equation 33. Vapor pressure deficit from saturation and actual water vapor pressure.

Relative humidity (RH Pa Pa⁻¹) is the proportion of the air's water capacity that is already occupied by water vapor. This is calculated as the ratio of actual (E_a kPa) to saturation (E_{sat} kPa) water vapor pressure (Equation 34).

$$RH = \frac{E_a}{E_{sat}}$$

Equation 34. Relative humidity from actual and saturation water vapor pressure.

6.3.3.4 Priestley-Taylor

The slope of the saturation to vapor pressure curve (Δ) is calculated from an exponential relationship with air temperature (T_a) (Equation 35).

$$\Delta = \frac{4098 * e^{\left(\frac{17.27 * T_a}{T_a + 237.7}\right)}}{(T_a + 237.3)^2}$$

Equation 35. Priestley-Taylor slope of the saturation vapor pressure curve from air temperature.

Two constants are used in the Priestley-Taylor equation, the Priestley-Taylor alpha (α) 1.26 and the psychrometric constant (γ) 0.0662 Pa K⁻¹.

The Priestley-Taylor formula is used to determine the potential amount of energy that can evaporate water. Of the energy that is available to evaporate water at the surface, net radiation (R_n W m⁻²) excluding soil heat flux (G W m⁻²), the Priestley-Taylor formula scales this down to potential evapotranspiration (PET W m⁻²) (Equation 36) (Priestley & Taylor, 1972).

$$PET = \alpha * \frac{\Delta}{\Delta + \gamma} * (R_n - G)$$

Equation 36. Potential evapotranspiration using Priestley-Taylor without constraints.

6.3.3.5 Constraints

The PT-JPL model imposes a set of proportional biophysical constraints on the Priestley-Taylor model of latent heat flux based on humidity, temperature, and vegetation. These constraints allow actual latent heat flux to be calculated from potential latent heat flux in partitions. These constraints are calculated at the monthly scale from monthly surface meteorology and vegetation.

Relative surface wetness (f_{wet}) is defined as the fourth power of relative humidity (RH) (Equation 37) (Fisher, Tu, & Baldocchi, 2008). This measure of humidity represents the amount of moisture on plants and soil, which evaporates from soil but prevents plants from needing to transpire (Equation 37) (Fisher, Tu, & Baldocchi, 2008).

$$f_{wet} = RH^4$$

Equation 37. Relative surface wetness from relative humidity.

Green canopy fraction (f_g) is defined as the ratio of absorbed (f_{APAR}) to intercepted (f_{IPAR}) photosynthetically active radiation (Equation 38) (Fisher, Tu, & Baldocchi, 2008).

$$f_g = \frac{f_{APAR}}{f_{IPAR}}$$

Equation 38. Green canopy fraction as the ratio of absorbed to intercepted photosynthetically active radiation.

Plant temperature constraint (f_T) is determined by air temperature (T_a) and optimum temperature (T_{opt}) (Equation 39) (Fisher, Tu, & Baldocchi, 2008).

$$f_T = e^{-\left(\frac{T_a - T_{opt}}{T_{opt}}\right)^2}$$

Equation 39. Plant temperature constraint from air temperature.

Plant moisture constraint is given by the ratio of absorbed photosynthetically active radiation (f_{APAR}) to maximum absorbed photosynthetically active radiation ($f_{APARmax}$) (Equation 40) (Fisher, Tu, & Baldocchi, 2008).

$$f_M = \frac{f_{APAR}}{f_{APARmax}}$$

Equation 40. Plant moisture constraint from absorbed photosynthetically active radiation.

Soil moisture is a volumetric ratio of water to soil. At the monthly temporal scale, there is a strong relationship between humidity and soil moisture. The soil moisture constraint (f_{SM} $m^3 m^{-3}$) is calculated from relative humidity (RH) and vapor pressure deficit (VPD kPa) (Equation 41) (Fisher, Tu, & Baldocchi, 2008). The RH and VPD used in this calculation are ideally derived from monthly values of near-surface air temperature and humidity. In production of an operational near-real time data product, the average of the past two weeks is used.

$$f_{SM} = RH^{VPD}$$

Equation 41. Soil moisture constraint from relative humidity and vapor pressure deficit.

6.3.3.6 Net Radiation Partitioning

PT-JPL partitions net radiation between the soil and the canopy. Soil net radiation (R_{ns} W m⁻²) is partitioned from total net radiation (R_n W m⁻²) using leaf area index (LAI) (Equation 42) (Fisher, Tu, & Baldocchi, 2008).

$$R_{ns} = R_n * e^{(-0.6*LAI)}$$

Equation 42. Formula to partition net radiation to the soil from total net radiation using leaf area index.

Net Radiation to the canopy (R_{nc} W m⁻²) is assumed to be the difference of total net radiation (R_n W m⁻²) and net radiation to the soil (R_{ns} W m⁻²) (Equation 43) (Fisher, Tu, & Baldocchi, 2008).

$$R_{nc} = R_n - R_{ns}$$

Equation 43. Formula for net radiation to the canopy from total net radiation and net radiation to the soil.

6.3.3.7 Canopy Transpiration

Canopy transpiration (LE_c W m⁻²) is calculated using the Priestley-Taylor equation with net radiation to the canopy (R_{nc} W m⁻²) as the source of energy, constrained by relative surface wetness (f_{wet}), green canopy fraction (f_g), and plant temperature (f_T) and moisture (f_M) constraints (Equation 44) (Fisher, Tu, & Baldocchi, 2008).

$$LE_c = (1 - f_{wet}) * f_g * f_T * f_M * \alpha * \frac{\Delta}{\Delta + \gamma} * R_{nc}$$

Equation 44. Formula for canopy transpiration, applying relative surface wetness, green canopy fraction, plant temperature and moisture constraints, and net radiation to the canopy to the Priestley-Taylor equation.

6.3.3.8 Interception Evaporation

Interception evaporation (LE_i $W m^{-2}$) is calculated using the Priestley-Taylor equation with relative surface wetness (f_{wet}) as the only constraint and net radiation to the canopy (R_{nc} $W m^{-2}$) as the source of energy (Equation 45) (Fisher, Tu, & Baldocchi, 2008).

$$LE_i = f_{wet} * \alpha * \frac{\Delta}{\Delta + \gamma} * R_{nc}$$

Equation 45. Formula for interception evaporation, applying relative surface wetness and net radiation to the canopy to the Priestley-Taylor equation.

6.3.3.9 Soil Evaporation

Soil evaporation (LE_s $W m^{-2}$) is calculated using the Priestley-Taylor equation with the difference of net radiation to the soil (R_{ns} $W m^{-2}$) and soil heat flux (G $W m^{-2}$) as the source of energy available to evaporate soil moisture, and relative surface wetness (f_{wet}) and soil moisture (f_{SM}) as constraints (Equation 46) (Fisher, Tu, & Baldocchi, 2008).

$$LE_s = (f_{wet} + f_{SM} * (1 - f_{wet})) * \alpha * \frac{\Delta}{\Delta + \gamma} * (R_{ns} - G)$$

Equation 46. Formula for soil evaporation, applying relative surface wetness, soil moisture constraint, net radiation to the soil, and soil heat flux to the Priestley-Taylor equation.

6.3.3.10 Latent Heat Flux

Instantaneous latent heat flux at the time of observation is composed by the sum of the partitions (Equation 50) (Fisher, Tu, & Baldocchi, 2008).

$$LE = LE_c + LE_i + LE_s$$

Equation 47. Total instantaneous latent heat flux from sum of partitions.

6.3.3.11 Evaporative Stress Index

Evaporative Stress Index (ESI) represents the relationship between actual and potential evapotranspiration. There are multiple definitions of this index in use, but ESI as used in

this project is the simple ratio of instantaneous latent heat flux to potential evapotranspiration (Equation 48).

$$ESI = \frac{LE}{PET}$$

Equation 48. Evaporative Stress Index from latent heat flux and potential evapotranspiration.

6.3.3.12 Daily Integration of Latent Heat Flux

Latent heat flux at the daily temporal scale is estimated by assuming the evaporative fraction (EF) (Equation 49) at the time of observation remains constant during daylight hours.

$$EF = \frac{LE}{R_n - G}$$

Equation 49. Evaporative fraction as ratio of latent heat flux to available energy.

Daily latent heat flux is obtained by applying this evaporative fraction to the daily integration of net radiation (Equation 50).

$$LE_d = EF * R_{nd}$$

Equation 50. Daily latent heat flux from evaporative fraction applied to daily integrated net radiation.

6.3.4 Water Use Efficiency

Latent heat flux represents evapotranspiration in terms of a rate of transfer of energy into water as watts per square meter. Watts are a rate of joules per second. To accumulate this rate over the course of the day, latent heat flux (LE_d) is multiplied by the number of seconds of daylight (Equation 51). To convert this amount of energy into an amount of water, a latent heat of vaporization of 2.45 million joules per kilogram is used (Equation 51). This results in daily evapotranspiration (ET_d) in kilograms of water evaporated per square meter

over the course of daylight (Equation 51). This is equivalent to change in height of water in millimeters.

$$ET_d = LE_d * \frac{DL * 3600}{2450000}$$

Equation 51. Daily evapotranspiration in kilograms from daily latent heat flux.

Water Use Efficiency (WUE) describes the relationship between rates of photosynthesis and evapotranspiration. WUE is calculated as the ratio of GPP in grams of carbon stored per kilograms of water evaporated (Equation 52).

$$WUE = \frac{GPP}{ET_d}$$

Equation 52. Water Use Efficiency as the ratio of gross primary production in grams of carbon to evapotranspiration in kilograms of water.

6.3.5 Uncertainty

Uncertainty for PT-JPL latent heat flux is provided by comparison to two additional evapotranspiration models, Penman-Monteith (Mu, Zhao, & Running, MODIS Global Terrestrial Evapotranspiration (ET) Product (NASA MOD16A2/A3) Algorithm Theoretical Basis Document Collection 5, 2013) and the Surface Energy Balance System (3.2.1). The standard deviation across the three model outputs is considered as the uncertainty of the PT-JPL estimation.

7 Dissemination

This data product pipeline is paired with a WebGIS system for dissemination. Technologies used in this system include Apache Tomcat, GeoServer, and Django, on the server side and Leaflet on the client side. These open-source, community-driven tools are well-established standards in the web design industry.

Apache Tomcat is used as the web server to deploy GeoServer because of its support for Cross-Origin Resource Sharing (CORS). The PT-JPL data pipeline transmits its output to GeoServer using POST requests, and GeoServer stores this data internally as GeoTIFF files. This method of hosting is preferable to using a PostGIS database, because these files can be directly served for the user to download over HTTP in a format that is readily compatible with desktop analysis software such as ArcGIS and QGIS. GeoServer uses the Web-Mapping Service (WMS) protocol to serve this data to the WebGIS system.

The WebGIS system used for the web interface is Leaflet, a JavaScript library that runs in the user's browser to display a map. A base map provided by Stamen is used as the basis for this map. Leaflet makes WMS requests to GeoServer for raster data interlaced to the map's current zoom level and viewing extent. GeoServer queries and renders this data to a color map and transmits it in Portable Network Graphics (PNG) format to Leaflet, which overlays it on the base map in the user's browser. The user can switch between raster overlays on top of this base map, including evapotranspiration, land-surface temperature, NDVI, and albedo, enabling comprehensive surface condition analysis.

Raster zonal statistics are implemented using the python Django framework. This is preferable to the Ruby on Rails framework because python has extensive geospatial support, including GDAL. The statistics server accepts AJAX requests containing the

coordinates of a polygon. The appropriate GeoTIFF is opened from *GeoServer*'s data directory, and raster data are selectively read within the bounding box of the target polygon. Statistics for these data are plotted using python's standard *matplotlib* visualization library. This plot is encoded into a base64 data URL and returned in the AJAX response to be displayed over the map and saved for future reference.

To enable the user to define regions of interest (ROIs), the *Leaflet.draw* plugin is integrated into the user experience. The user can draw rectangles and irregular polygons, such as municipal or land ownership boundaries. Once drawn, the coordinates defining an ROI are transmitted to the Django statistics server, and the plot returned in the AJAX response is displayed in the browser (Figure 22). To query single points of data on the map, the user can place a marker. All evapotranspiration values and statistics displayed include both an energy flux value in watts per square meter and a water flux value in millimeters per day to enable easy calculation of water resources. The date picker can be expanded to a full calendar to select target dates, and ROIs persist on the map when the date is changed to allow analysis of change over time.

As an added convenience to the user, two locators are included on the map controls. One locator estimates the coordinates of the user's location and pans to this location on the map, which is a valuable tool for on-site inspection using mobile devices. The other locator accepts an address or place name and uses the Google Geocoding API to determine a coordinate to pan to on the map. This allows water resource managers to target specific properties by address.

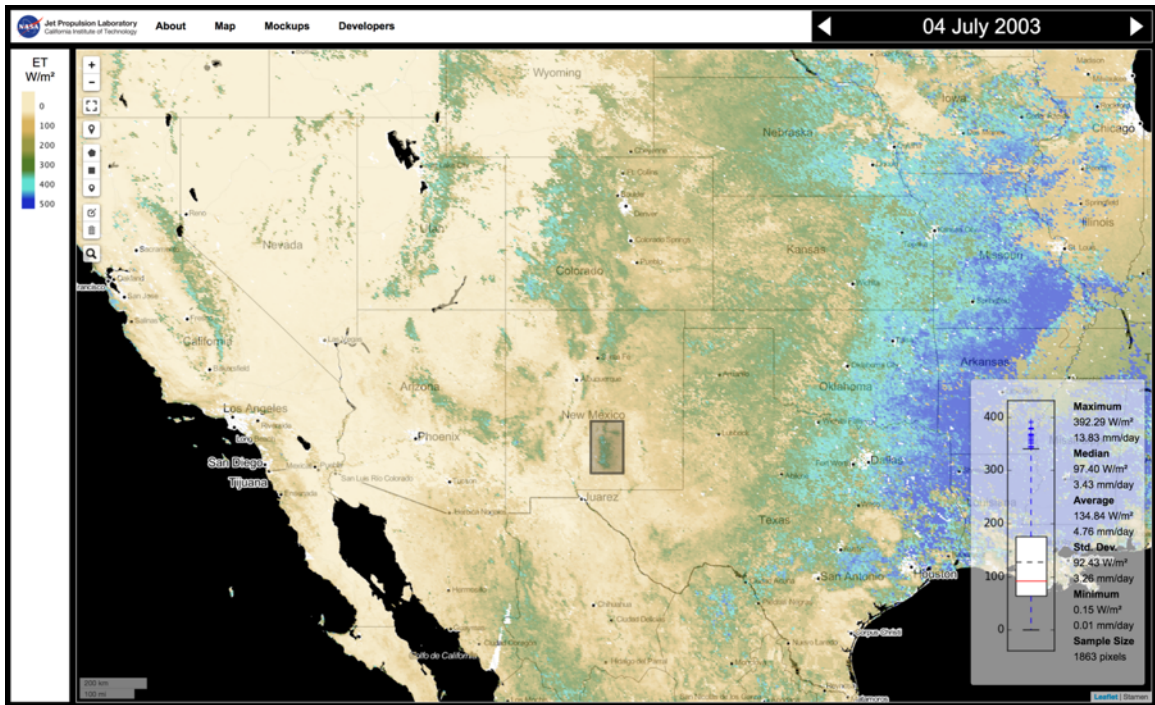


Figure 22. Example of WebGIS dissemination system with boxplot queried by hand-drawn region of interest.

8 Demonstration of Output

This section demonstrates the data produced by the pipeline using New Mexico as a study area. The pipeline was run for MODIS land tiles h08v05 and h09v05, covering the state of New Mexico, for every day from 2013 through 2015. To demonstrate a broad assessment of this region over both space and time, the instantaneous latent heat flux partitions from each morning in the produced dataset were aggregated by month and season, projected to UTM Zone 13 North, and clipped to the boundaries of New Mexico. These seasonal maps (Figure 26) reveal the county-scale spatial distribution of latent heat flux partitions as well as their seasonality and inter-annual variability. The monthly maps were spatially aggregated to a table to present seasonality and inter-annual variability at higher temporal resolution (Figure 23).

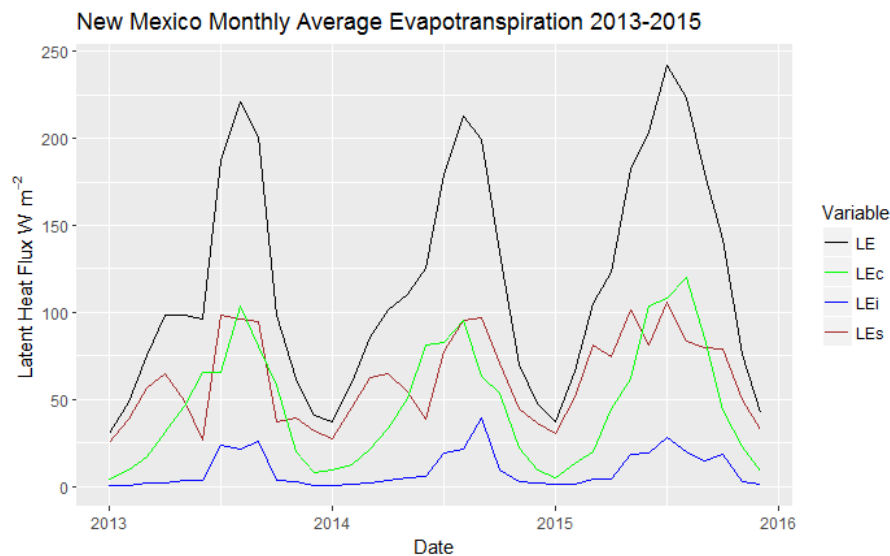


Figure 23. Monthly trends of New Mexico evapotranspiration from 2013 to 2015 with interception in blue, transpiration in green, soil evaporation in brown, and total latent heat flux in black.

Latent heat flux ground observations from the Valles Caldera Mixed Conifer (US-Vcm) eddy covariance site was used to demonstrate the accuracy and uncertainty of the model output. An ensemble timeline of latent heat flux from PT-JPL, Penman Monteith (PM-MOD), and SEBS was compared to the US-Vcm eddy covariance tower (Figure 24),

demonstrating that the ground observations were well within the model output uncertainty.

A scatterplot (Figure 25) of monthly aggregates of latent heat flux between PT-JPL and US-Vcm site show good correspondence ($R^2 = 0.83$, $\rho = 0.91$) as well.

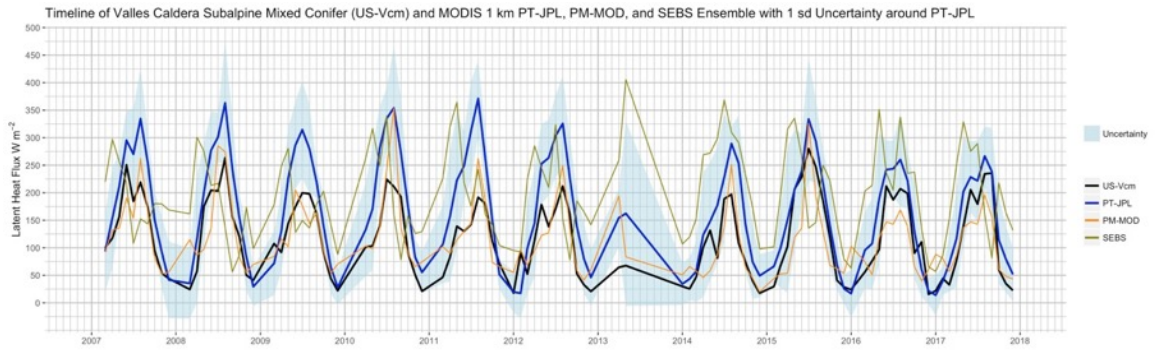


Figure 24. Eddy covariance measurement of latent heat flux at US-Vcm site compared to New Mexico record of MODIS PT-JPL, including uncertainty.

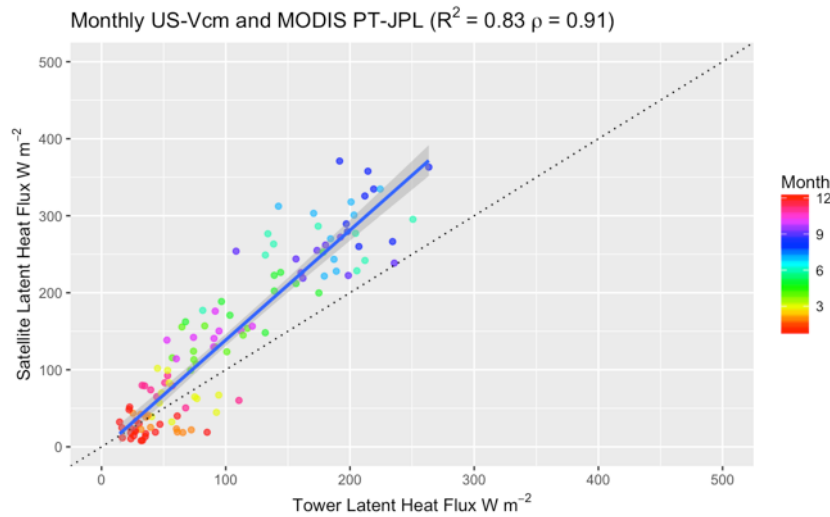


Figure 25. Scatterplot comparing monthly aggregates of latent heat flux between the US-Vcm eddy covariance site and MODIS PT-JPL.

Seasonal Trends of New Mexico Evapotranspiration

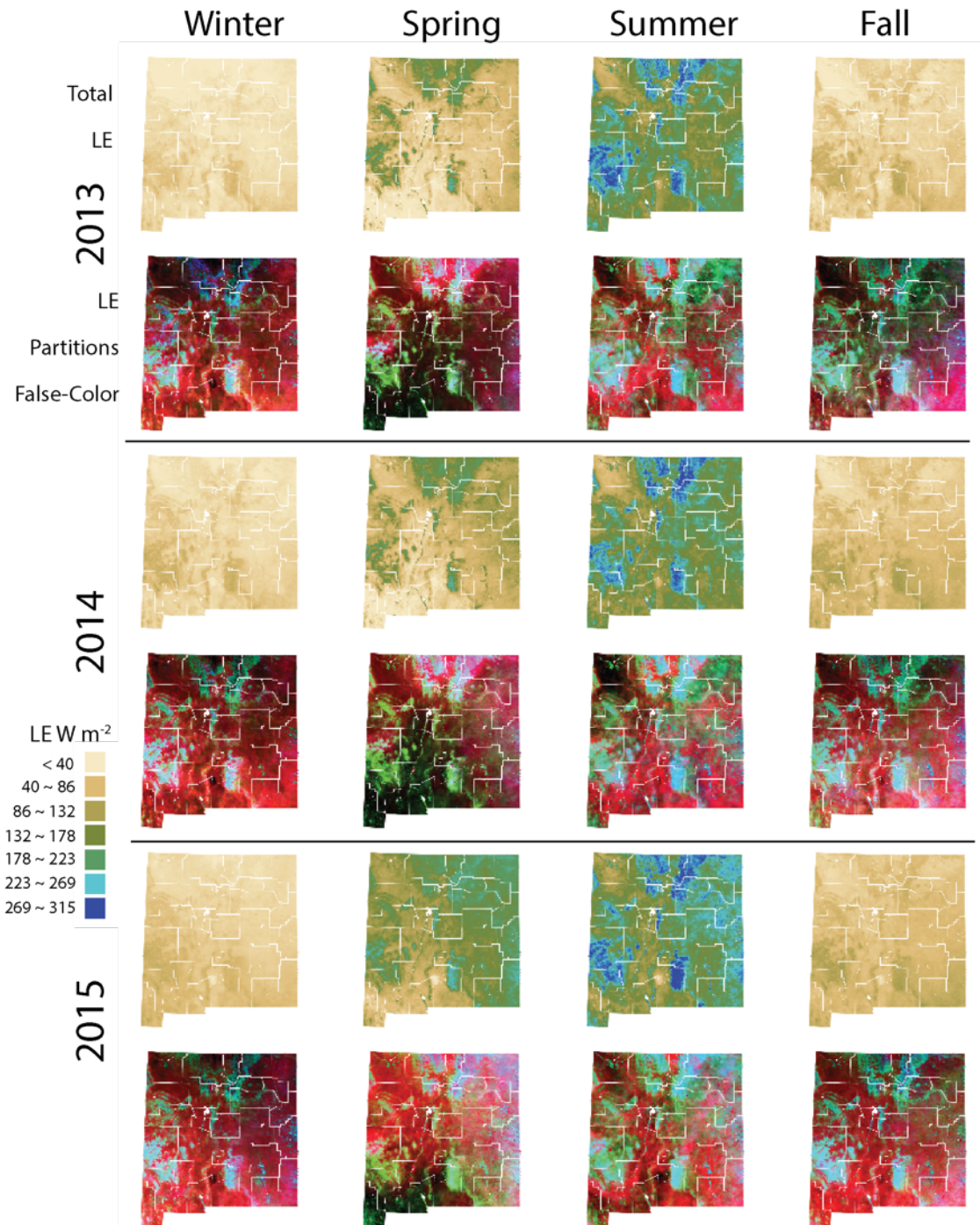


Figure 26. Time-series of seasonal trends in New Mexico from 2013 to 2015. The first, third, and fifth rows are pseudo-color plots of total latent heat flux at the time of Terra overpass, aggregated by month. The second, fourth, and sixth rows are corresponding false-color plots with soil evaporation in red, canopy transpiration in green, and interception in blue. New Mexico county boundaries are demarcated in white.

9 Applications

A partnership between the California State University Northridge, NASA's Western Water Applications Office (WWAO) at the Jet Propulsion Laboratory, and the New Mexico Office of the State Engineer enabled stakeholder outreach with New Mexico water management. These outreach efforts have developed a set of decision-making contexts for the use of remotely sensed evapotranspiration in New Mexico. Potentially high impact use-cases focused on agriculture and forest management are summarized here.

9.1 Agriculture and Water Rights

Stakeholder engagement with the New Mexico Office of the State Engineer showed that agricultural applications in statewide water management relate largely to the management of water rights and could be informed by high spatial resolution remote sensing imagery of evapotranspiration. There is potential to inform the decision-making contexts of priority administration, active water resource management, and water rights transfers using the spatial capabilities of Landsat PT-JPL (Figure 27). In times of water scarcity, priority administration is employed to ensure that senior water rights holders have access to water, and junior water rights holders may be required to reduce irrigation. Access to Landsat evapotranspiration data can help water managers ensure compliance with priority administration. In some districts, an alternative response to scarcity is available called active water resource management (AWRM). Use of AWRM prevents abrupt curtailing of water use by negotiating shortage sharing agreements. Improvement in the monitoring and management of water rights, including prioritization and subsidization can help save water in times of scarcity and ensure availability of water for interstate compact deliveries.

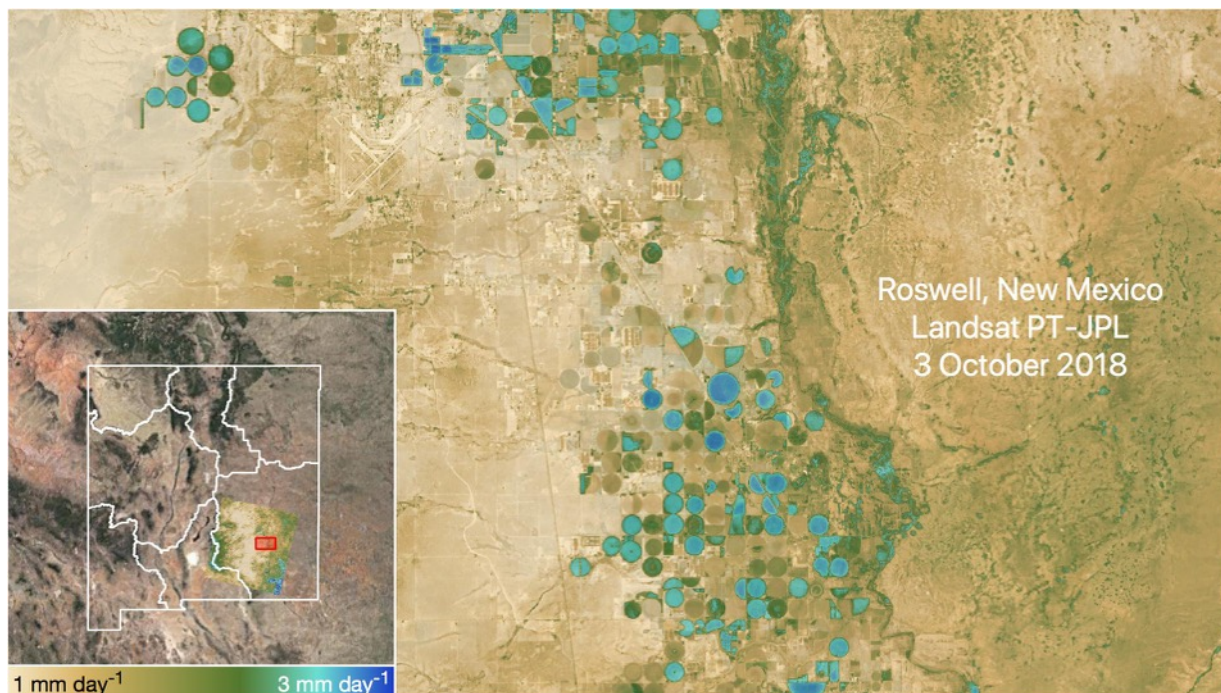


Figure 27. Example of high-resolution evapotranspiration imagery for monitoring irrigation in New Mexico.

There is also the potential for utilizing long-term timeseries of Landsat evapotranspiration spanning multiple decades to inform the decision-making process of granting water rights transfer requests. When a water rights holder wants to sell their water right, the water right transfer request process requires demonstration of long-term continuous beneficial use. Current practices rely on examining archives of RGB aerial imagery. Continuous beneficial use can much better be determined by a historical record of high-resolution evapotranspiration data. Having access to this data may allow water management to prevent the sale of extremely over-valued water rights, which saves water and money.

9.2 Forest and Riparian Management

Stakeholder engagement in New Mexico revealed that access to remotely sensed evapotranspiration data can inform decisions in the management of vegetation in forests and riparian areas. Remotely sensed evapotranspiration data can help identify areas of forests that are severely dry and prone to catastrophic fire. Preventing such fires helps

prevent erosion and debris flow in rivers. Conversely, identifying abnormally high areas of evapotranspiration in forests can aid controlling the water storage and loss of forests and resulting streamflow. These data may also be useful in identifying over-crowded areas of forest that prevent the formation of snowpack, potentially increasing available snowpack in the water supply.

10 Conclusion

Monitoring the spatial distribution of water transfer in land-atmosphere interaction over time through remote sensing of evapotranspiration can better inform water and land managers in the protection of natural resources. The evapotranspiration monitoring system demonstrated here will be the first of its kind to provide assessments to changes in water availability, use, and land-surface aridity with the combined strengths of the high temporal resolution of MODIS and the high spatial resolution of Landsat. Near real-time interactive access to this information will provide state-level natural resource managers a tool to monitor, anticipate, and mitigate issues relating to the water supply.

The ability to watch over the Earth from space and peer beyond the visible bands of light that we can see with our eyes into environmental variables ascertained from the electromagnetic spectrum through the progress of satellite technology is one of the greatest accomplishments of mankind. This accomplishment serves the purposes of both advancing scientific inquiry into the inner functioning of nature as well as providing applied decision-making information that affects our daily lives.

Bibliography

- Allen, R. G., Pereira, L. S., Raes, D., & Smith, M. (2006). *FAO Irrigation and Drainage Paper No. 56 Crop Evapotranspiration*. FAO.
- Allouche, J. (2011). The sustainability and resilience of global water and food systems: *Food Policy*, 36, 53-58.
- Amazon Web Services. (2017). *Landsat on AWS*. Retrieved from Amazon Web Services: <https://aws.amazon.com/public-datasets/landsat/>
- American Meteorological Society. (2014, 5 22). *gas constant*. Retrieved from AMERICAN METEOROLOGICAL SOCIETY glossary of meteorology: http://glossary.ametsoc.org/wiki/Gas_constant
- Anderson, M. C., Kustas, W. P., Norman, J. M., Hain, C. R., Mecikalski, J. R., Schultz, L., . . . Gao, F. (2011). Mapping daily evapotranspiration at field to continental scales using geostationary and polar orbiting satellite imagery. *Hydrol. Earth Syst. Sci.*, 15, 223–239. doi:10.5194/hess-15-223-2011
- Arizona State University. (2017). *Snacking on Sunlight*. Retrieved from Arizona State University School of Life Sciences: <https://askabiologist.asu.edu/cam-plants>
- Becker-Reshef, I., Justice, C., Sullivan, M., Vermote, E., Tucker, C., Anyamba, A., . . . Doorn, B. (2010). Monitoring Global Croplands with Coarse Resolution Earth Observations: The Global Agriculture Monitoring (GLAM) Project. *Remote Sensing*, 2, 1589-1609. doi:10.3390/rs2061589
- Biazin, B., & Sterk, G. (2012, 9 21). Drought vulnerability drives land-use and land cover changes in the Rift Valley. *Agriculture, Ecosystems and Environment*, 164, 100-113.
- Boddy, J. (2016, 12 21). *As record Appalachian wildfires fizzle out, scientists look to learn from the destruction*. (AAAS) Retrieved from Science: <http://www.sciencemag.org/news/2016/12/record-appalachian-wildfires-fizzle-out-scientists-look-learn-destruction>
- Breshears, D. D., Knapp, A. K., Law, D. J., Smith, M. D., & Twidwell, D. (2016). Rangeland Responses to Predicted. (S. f. Management, Ed.) *Rangelands*, 38(4), 191-196. doi:0.1016/j.rala.2016.06.009
- Chen, Y., Xia, J., Liang, S., Feng, J., Fisher, J. B., Li, X., . . . Yuan, W. (2014). Comparison of satellite-based evapotranspiration models over terrestrial ecosystems in China. *Remote Sensing of Environment*, 140, 279-293.
- Chow, L. (2016, 11 21). *102 Million Trees Have Died in California's Drought*. Retrieved from EcoWatch: <http://www.ecowatch.com/dead-trees-california-drought-2103497094.html>
- EPA. (2016, 4). *United States Environmental Protection Agency*. Retrieved 3 16, 2017, from Climate Change Indicators in the United States: <https://www3.epa.gov/climatechange/science/indicators/ecosystems/wildfires.html>
- Ershadi, A., McCabe, M. F., Evans, J., Chaney, N. W., & Wood, E. F. (2014). Multi-site evaluation of terrestrial evaporation models using FLUXNET data. *Agricultural and Forest Meteorology*, 187, 46-61.
- Fisher, J. B. (2012, 7 10). Land-Atmosphere Interactions: Evapotranspiration. In S.-V. B. Heidelberg, & D. E. Njoku (Ed.), *Encyclopedia of Remote Sensing*. Springer-Verlag Berlin Heidelberg. doi:10.1007/SpringerReference_327146
- Fisher, J. B. (2013, 5). *RHEAS*. Retrieved from Western States Water Council: <http://www.westernstateswater.org/wp-content/uploads/2013/05/Fisher.pdf>

- Fisher, J. B., Tu, K. P., & Baldocchi, D. B. (2008). Global estimates of the land-atmosphere water flux based on monthly AVHRR and ISLSCP-II data, validated at 16 FLUXNET sites. *Remote Sensing of Environment*, 112, 901-919.
- Friedl, R., & Granger, S. (2016, 9 29). *Western Water Applications Office*. Retrieved from Western States Water Council: http://www.westernstateswater.org/wp-content/uploads/2016/03/092916_WWAO_WSWC_Friedl.pdf
- Gao, F., Masek, J., Schwaller, M., & Hall, F. G. (2006, 8). On the Blending of the Landsat and MODIS Surface Reflectance: Predicting Daily Landsat Surface Reflectance. *IEEE Transactions on Geoscience and Remote Sensing*, 44(8). doi:10.1109/TGRS.2006.872081
- Goddard Space Flight Center. (2016, 12 2). *MODIS Grids*. Retrieved from MODIS Land Team: https://modis-land.gsfc.nasa.gov/MODLAND_grid.html
- Goddard Space Flight Center. (2017, 1 15). *NOAA Surface Type EDR*. Retrieved from VIIRS Land Team: <https://viirsland.gsfc.nasa.gov/Products/LandcoverEDR.html>
- Goddard Space Flight Center. (2017). *Precipitation Education*. Retrieved 3 19, 2017, from Precipitation Measurement Missions: <https://pmm.nasa.gov/education/water-cycle>
- Hanjra, M. A., & Qureshi, M. E. (2010, 5 19). Global water crisis and future food security in an era of climate change. *Food Policy*, 35, 365-377.
- Hao, Z., AghaKouchak, A., Nakhjiri, N., & Farahmand, A. (2014, 3 11). Global integrated drought monitoring and prediction system. *Scientific Data*, 1(140001). doi:10.1038/sdata.2014.1
- Huete, A., Justice, C., & Leeuwen, W. v. (1999). *MODIS VEGETATION INDEX (MOD 13) ALGORITHM THEORETICAL BASIS DOCUMENT*. NASA. Retrieved from http://modis.gsfc.nasa.gov/data/atbd/atbd_mod13.pdf
- Huntington, T. G. (2005, 7 7). Evidence for intensification of the global water cycle: Review and synthesis. *Journal of Hydrology*, 319, 83-95.
- Institute for Veterinary Public Health. (2017). Retrieved from WORLD MAPS OF KÖPPEN-GEIGER CLIMATE CLASSIFICATION: <http://koeppen-geiger.vu-wien.ac.at>
- IPCC. (2014). *Climate Change 2014: Impacts, Adaptation, and Vulnerability. Part A: Global and Sectoral Aspects. Contribution of Working Group II to the Fifth Assessment Report of the Intergovernmental Panel on Climate Change*. (p. 1132). Cambridge University Press.
- Jiménez-Muñoz, J. C., Sobrino, J. A., Skokovic, D., Mattar, C., & Cristóbal, J. (2014, 10 10). Land Surface Temperature Retrieval Methods From Landsat-8 Thermal Infrared Sensor Data. *IEEE GEOSCIENCE AND REMOTE SENSING LETTERS*, 11, 1840-1843.
- Kobayashi, H., & Iwabuchi, H. (2008). A coupled 1-D atmosphere and 3-D canopy radiative transfer model for canopy reflectance, light environment, and photosynthesis simulation in a heterogeneous landscape. *Remote Sensing of Environment*, 112, 173-185. doi:<http://dx.doi.org/10.1016/j.rse.2007.04.010>
- Kobayashi, H., Baldocchi, D. D., Ryu, Y., Chen, Q., Ma, S., Osuna, J. L., & Ustin, S. L. (2012). Modeling energy and carbon fluxes in a heterogeneous oak woodland: A three-dimensional approach. *Agricultural and Forest Meteorology*, 152, 83-100. doi:<http://dx.doi.org/10.1016/j.agrformet.2011.09.008>
- Kustas, W. P., Norman, J. M., Anderson, M. C., & French, A. N. (2003, 1 18). Estimating subpixel surface temperatures and energy fluxes from the vegetation index-radiometric temperature relationship. *Remote Sensing of Environment*, 85, 429-440. doi:10.1016/S0034-4257(03)00036-1
- Langley Advanced Research Center. (2016, 20 28). *Earth's Energy Budget Poster*. Retrieved from NASA LaRC SD EPO: https://science-edu.larc.nasa.gov/energy_budget/

- Lawrence, M. G. (2005). The relationship between relative humidity and the dewpoint temperature in moist air: A simple conversion and applications. *Bull. Amer. Meteor. Soc.*, 86, 225-233. doi:<http://dx.doi.org/10.1175/BAMS-86-2-225>
- Levy, R. C., Remer, L. A., Tanre, D., Mattoo, S., & Kaufman, Y. J. (2009). *ALGORITHM FOR REMOTE SENSING OF TROPOSPHERIC AEROSOL OVER DARK TARGETS FROM MODIS*. ATBD, NASA. Retrieved from http://modis-atmos.gsfc.nasa.gov/_docs/ATBD_MOD04_C005_rev2.pdf
- Liou, Y.-A., & Kar, S. K. (2014). Evapotranspiration Estimation with Remote Sensing and Various Surface Energy Balance Algorithms—A Review. *Energies*, 7, 2821-2849. doi:10.3390/en7052821
- Menzel, P. W., Frey, R. A., & Baum, B. A. (2010). *CLOUD TOP PROPERTIES AND CLOUD PHASE ALGORITHM THEORETICAL BASIS DOCUMENT*. ATBD, NASA. Retrieved from http://modis-atmos.gsfc.nasa.gov/_docs/CTP_ATBD_oct10.pdf
- Morton, J. F. (2007, 12 11). The impact of climate change on smallholder and subsistence agriculture. (W. Easterling, Ed.) *PNAS*, 104(5), 19680–19685. doi:10.1073/pnas.0701855104
- Mu, Q., Zhao, M., & Running, S. W. (2011). Improvements to a MODIS global terrestrial evapotranspiration algorithm. *Remote Sensing of Environment*, 115, 1781-1800.
- Mu, Q., Zhao, M., & Running, S. W. (2013). *MODIS Global Terrestrial Evapotranspiration (ET) Product (NASA MOD16A2/A3) Algorithm Theoretical Basis Document Collection 5*. The University of Montana, College of Forestry and Conservation. Missoula, MT: National Aeronautics and Space Administration. Retrieved from http://www.ntsg.umt.edu/sites/ntsg.umt.edu/files/MOD16_ATBD.pdf
- NOAA Earth System Research Laboratory. (2017). *NCEP/NCAR Reanalysis 1: Surface*. Retrieved from Earth System Research Laboratory Physical Sciences Division: <https://www.esrl.noaa.gov/psd/data/gridded/data.ncep.reanalysis.surface.html>
- Olmedo, G. F., Ortega-Farias, S., Fonseca-Luengo, D., de la Fuente-Saiz, D., & Peñailillo, F. F. (2017). *Actual Evapotranspiration with Energy Balance Models*. Retrieved from <https://CRAN.R-project.org/package=water>
- Priestley, C. H., & Taylor, R. J. (1972). On the Assessment of Surface Heat Flux and Evaporation Using Large-Scale Parameters. *Monthly Weather Review*, 100(2), 81-92.
- Ryu, Y., Baldocchi, D. D., Kobayashi, H., van Ingen, C., Li, J., Black, T. A., . . . Roupsard, O. (2011). Integration of MODIS land and atmosphere products with a coupled-process model to estimate gross primary productivity and evapotranspiration from 1 km to global scales. *GLOBAL BIOGEOCHEMICAL CYCLES*, 25(GB4017). doi:10.1029/2011GB004053
- Saleem, M. U. (2016, 2 29). Gnomon Assessment for Geographic Coordinate, Solar Horizontal & Equatorial Coordinates, Time of Local Sunrise, Noon, Sunset, Direction of Qibla, Size of Earth & Sun for Lahore Pakistan. *Open Journal of Applied Sciences*, 100-111.
- Sayre, N. F., McAllister, R. R., Bestelmeyer, B. T., Moritz, M., & Turner, M. D. (2013). Earth Stewardship of rangelands: coping with ecological, economic, and political marginality. *Frontiers in Ecology and the Environment*, 11(7), 348-354. doi:10.1890/120333
- Seemann, S. W., Borbas, E. E., Li, J., Menzel, W. P., & Gumley, L. E. (2006). *MODIS ATMOSPHERIC PROFILE RETRIEVAL ALGORITHM THEORETICAL BASIS DOCUMENT*. NASA. Retrieved from http://modis-atmos.gsfc.nasa.gov/_docs/MOD07MYD07ATBDC005.pdf
- Strahler, A. H., Lucht, W., Schaaf, C. B., Tsang, T., Gao, F., Li, X., . . . Bransley, M. J. (1999). *MODIS BRDF/Albedo Product: Algorithm Theoretical Basis Document Version 5.0*. NASA. Retrieved from http://modis-land.gsfc.nasa.gov/pdf/atbd_mod09.pdf
- The World Bank. (2017). *The World Bank*. Retrieved from <http://www.worldbank.org>

- United States Department of Energy. (2008). *Carbon Cycling and Biosequestration: Integrating Biology and Climate Through Systems Science; Report from the March 2008 Workshop, DOE/SC-108*. United States Department of Energy Office of Science.
- United States Drought Monitor. (2017). *Tabular Data Archive*. Retrieved from United States Drought Monitor: <http://droughtmonitor.unl.edu/MapsAndData/DataTables.aspx>
- USGS. (2016, 11 29). *Landsat Missions*. Retrieved from Using the USGS Landsat 8 Product: <https://landsat.usgs.gov/using-usgs-landsat-8-product>
- USGS. (2016, 11 29). *What are the band designations for the Landsat satellites?* Retrieved from Landsat Missions: <https://landsat.usgs.gov/what-are-band-designations-landsat-satellites>
- Verma, M., Fisher, J. B., Mallick, K., Ryu, Y., Kobayashi, H., Guillaume, A., . . . Stephens, G. (2016). Global daily surface net-radiation at 5 km from MODIS. *International Journal of Applied Observation and Geoinformation*.
- Vinukollu, R. K., Wood, E. F., Ferguson, C. R., & Fisher, J. B. (2010). Global estimates of evapotranspiration for climate studies using multi-sensor remote sensing data: Evaluation of three process-based approaches. *Remote Sensing of Environment*, 115, 801-823.
- Wan, Z. (1999). *MODIS Land-Surface Temperature Algorithm Theoretical Basis Document (LST ATBD)*. University of California, Santa Barbara, Institute for Computational Earth System Science. Retrieved from http://modis.gsfc.nasa.gov/data/atbd/atbd_mod11.pdf
- Westerling, A. L., Hidalgo, H. G., Cayan, D. R., & Swetnam, T. W. (2006, 8 18). Warming and Earlier Spring Increase Western U.S. Forest Wildfire Activity. *SCIENCE*, 313.
- Yale University. (2017). *How to convert Landsat DNs to albedo*. Retrieved from Yale University Center for Earth Observation: <http://yceo.yale.edu/how-convert-landsat-dns-albedo>
- Ziegler, A. D., Sheffield, J., Maurer, E. P., Nijssen, B., Wood, E. F., & Lettenmaier, D. P. (2003). Detection of Intensification in Global- and Continental-Scale Hydrological Cycles: Temporal Scale of Evaluation. *Journal of Climate*, 16(3), 535-547.